

---

# HEMORICA: A COMPREHENSIVE CT SCAN DATASET FOR AUTOMATED BRAIN HEMORRHAGE CLASSIFICATION, SEGMENTATION, AND DETECTION

---

**Kasra Davoodi\***

seyedkasra.davoodi@email.kntu.ac.ir

**Mohammad Hoseyni\***

mohammadhosini@email.kntu.ac.ir

**Javad Khoramdel**

j.khorramdel196@gmail.com

**Reza Barati<sup>†</sup>**

barati.r@iums.ac.ir

**Reihaneh Mortazavi<sup>†</sup>**

reihaneh.mortazavi@yahoo.com

**Amirhossein Nikoofard**

a.nikoofard@kntu.ac.ir

**Mahdi Aliyari-Shoorehdeli**

aliyari@eetd.kntu.ac.ir

**Jaber Hatam Parikhan<sup>‡</sup>**

hatam.j@iums.ac.ir

## ABSTRACT

Timely diagnosis of Intracranial hemorrhage (ICH) on Computed Tomography (CT) scans remains a clinical priority, yet the development of robust Artificial Intelligence (AI) solutions is still hindered by fragmented public data. To close this gap, we introduce **Hemorica**, a publicly available collection of 372 head-CT examinations acquired between 2012 and 2024. Each scan has been exhaustively annotated for five ICH sub-types—epidural (EPH), subdural (SDH), subarachnoid (SAH), intraparenchymal (IPH), and intraventricular (IVH)—yielding patient-wise and slice-wise classification labels, subtype-specific bounding boxes, two-dimensional pixel masks and three-dimensional voxel masks. A double-reading workflow, preceded by a pilot consensus phase and supported by neurosurgeon adjudication, maintained low inter-rater variability. Comprehensive statistical analysis confirms the clinical realism of the dataset. To establish reference baselines, standard convolutional and transformer architectures were fine-tuned for binary slice classification and hemorrhage segmentation. With only minimal fine-tuning, lightweight models such as MobileViT-XS achieved an F1 score of 87.8% in binary classification, whereas a U-Net with a DenseNet161 encoder reached a Dice score of 85.5% for binary lesion segmentation that validate both the quality of the annotations and the sufficiency of the sample size. Hemorica therefore offers a unified, fine-grained benchmark that supports multi-task and curriculum learning, facilitates transfer to larger but weakly labelled cohorts, and facilitates the process of designing an AI-based assistant for ICH detection and quantification systems.

**Keywords** Brain hemorrhage, Computed Tomography, Medical Imaging Dataset, Hemorrhage Classification, Hemorrhage Detection, Hemorrhage Segmentation, Deep Learning

## 1 Introduction

ICH has been recognized as a major global health burden, particularly in low- and middle-income countries, where it ranks among the leading causes of mortality and long-term disability in adults. Although hemorrhagic strokes are less prevalent than their ischemic counterparts, the overall social and economic consequences of ICH have been shown to be more profound [1]. As the second most common form of stroke, ICH constitutes a life-threatening neurological

---

\*Equal contribution

<sup>†</sup>Equal contribution

<sup>‡</sup>Corresponding author

emergency that disproportionately affects specific demographic groups and regions. Higher incidence rates have been consistently reported among older adults, males, and individuals residing in low- and middle-income countries, with Asian populations exhibiting a particularly elevated risk [2]. Several contributing factors have been identified, including advanced age, male sex, Asian ethnicity, chronic kidney disease, cerebral amyloid angiopathy, and cerebral microbleeds [2]. The severity of ICH is further underscored by its poor clinical outcomes, with a 40% mortality rate within the first month and over 50% within one year. Alarmingly, only 12% to 39% of survivors are able to regain long-term functional independence [2], reinforcing the urgent need for targeted prevention and intervention strategies.

ICH is categorized into five primary subtypes based on the location of bleeding: epidural hemorrhage (EPH), subdural hemorrhage (SDH), subarachnoid hemorrhage (SAH), intraparenchymal hemorrhage (IPH), and intraventricular hemorrhage (IVH). EPH and SDH are extra-axial hemorrhages, occurring outside the brain parenchyma, whereas SAH, IPH, and IVH are intra-axial, involving bleeding within the brain tissue or ventricular system. These subtypes differ in etiology, imaging characteristics, and clinical outcomes. EPH commonly appears as a biconvex hyperdense region on CT and is often associated with skull fractures. SDH varies in density based on chronicity and typically results from trauma or coagulopathy. SAH involves bleeding into the subarachnoid space, frequently due to trauma or ruptured aneurysms. IPH is characterized by bleeding directly into the brain parenchyma, often linked to hypertension, vascular abnormalities, or head injury. IVH, representing 0.31% of all strokes and 3.1% of spontaneous intracranial hemorrhages, involves nontraumatic bleeding within the brain's ventricular system and its surrounding ependymal lining, without clear involvement of brain tissue, and is commonly linked to high blood pressure, arteriovenous malformations, aneurysms, moyamoya disease, blood clotting disorders, or arteriovenous fistulas in adults, while being more frequent in premature infants [3, 4].

Timely and accurate diagnosis of ICH is crucial for initiating effective clinical intervention and reducing the likelihood of severe disability or death [5, 6]. Computed tomography (CT) has remained the standard imaging modality in emergency settings due to its rapid acquisition time and high diagnostic sensitivity in detecting acute intracranial bleeding [7, 8]. The manual process of diagnosing ICH lesions in CT scan radiographs has been regarded as time-consuming and dependent on the availability of trained specialists [5]. In addition to these limitations, traditional manual methods such as the ABC/2 approach, which is commonly used to estimate the volume of hemorrhagic lesions, have been shown to overestimate lesion size by approximately 30% [9]. However, with the advancement of AI-based assistants, computer-aided diagnosis can now be implemented in clinical settings to enhance both the efficiency and accuracy of diagnosis. Through automated segmentation of the lesion area, AI-based tools offer the potential for more precise calculation of hemorrhage volume, thereby addressing key limitations of manual diagnostic techniques.

The advancement of reliable AI-based diagnostic systems has been hindered by significant barriers, primarily due to fragmented and non-publicly accessible datasets. For instance, a deep learning model presented in [8] demonstrated a remarkable reduction of 96.3% in median diagnosis time compared to standard workflows. Nevertheless, the lack of open access to the underlying dataset has impeded reproducibility and broader implementation, thereby limiting the translational potential of such innovations. However, the promise of AI-driven solutions for ICH diagnosis is tightly linked to the availability of comprehensive, high-quality datasets—a need that remains largely unmet. Most existing datasets suffer from several critical limitations, including a relatively small number of CT scans and an insufficient volume of annotated studies to support the development of robust AI models. In many cases, the radiographic image quality is suboptimal, and the annotation protocols lack standardization, often relying on inconsistent or expedited labeling procedures. As a result, conflicts in final annotations are common, leading to reduced accuracy and reliability in the ground truth data, thereby limiting the generalizability and clinical applicability of trained models. A number of collections remain private [8, 10, 11, 12, 13, 14], hindering collaborative progress and benchmarking. Among publicly available resources, the CQ500 dataset [7] and the RSNA Intracranial Hemorrhage Detection Challenge dataset [15, 16] offer large sample sizes but lack fine-grained annotations—such as bounding boxes and segmentation masks—which are essential for interpretable model outputs and for enabling both 2D and 3D segmentation as well as object detection. Furthermore, some datasets provide only patient-level labels [7, 8] or slice-level annotations [15, 16], limiting a model's ability to accurately localize hemorrhagic lesions. Several more recent collections [17, 13, 14] fail to cover the full spectrum of hemorrhage subtypes, thereby restricting their utility in identifying specific bleeding categories. Although coarse bounding box annotations are available in certain datasets [17], no standardized test protocol has been established for benchmarking. Finally, some datasets suffer from small sample sizes [18, 11] and limited diversity in hemorrhage etiologies, further constraining their generalizability.

To bridge these gaps, **Hemorica** is introduced, a publicly available CT brain hemorrhage dataset with high-quality, fine-grained annotations spanning slice-level bounding boxes, 2D masks, and 3D voxel-level labels for multiple hemorrhage subtypes that has been gathered from Rasoul Akram hospital in Iran. In this paper, we conduct a comprehensive comparative statistical analysis between our dataset and existing public resources, highlighting how Hemorica overcomes prior limitations. We further demonstrate its versatility by defining a suite of computer vision tasks, including image classification and segmentation.

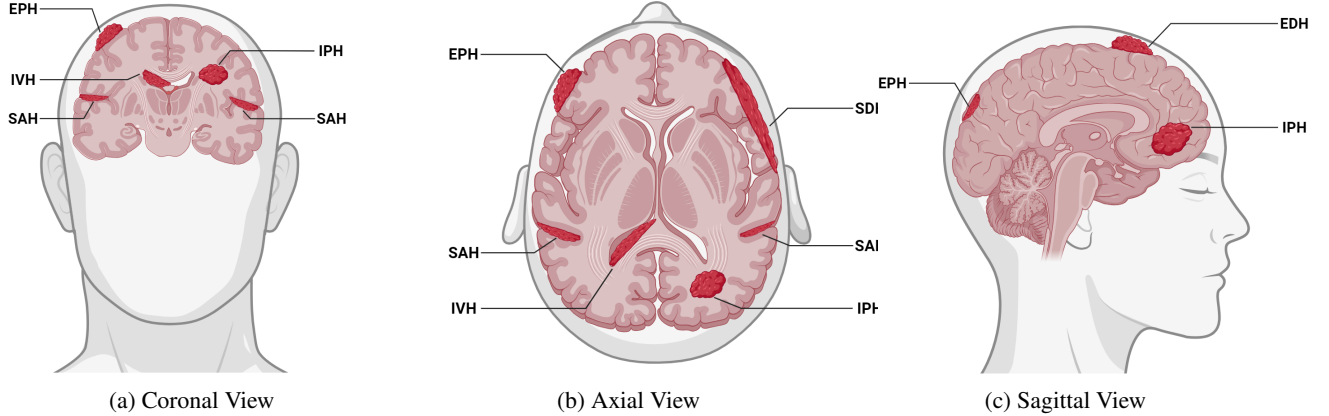


Figure 1: Different views for processing a CT scan and the locations of various hemorrhage subtypes

Beyond serving as a supervised benchmark, models pretrained on Hemorica can bootstrap high-quality pseudo-labels on other large-scale CT collections such as [7, 15, 16], thus enabling self-supervised and weakly supervised learning approaches to advance AI-driven brain hemorrhage diagnosis.

Our main contributions are summarized as follows:

1. In **Hemorica**, a comprehensive, publicly available CT dataset has been introduced, specifically for the diagnosis of multiple hemorrhage subtypes. The dataset includes slice-level classification labels for five major hemorrhage subtypes, patient-level diagnostic labels reflecting subtype presence, slice-level bounding boxes for subtype-specific hemorrhage localization, pixel-level 2D segmentation masks, 3D voxel-level annotations per subtype, and regression values estimating hemorrhage volume for each subtype.
2. A detailed statistical analysis of the dataset is performed, including subtype-wise distribution, lesion size variation, and class balance across slice and patient levels, and these characteristics are compared with existing public datasets to highlight the completeness and representativeness of the data.
3. A benchmark for hemorrhage subtype diagnosis—covering classification, detection, and segmentation—is established using standard deep learning architectures, and baseline results are provided to facilitate reproducible comparisons in future research.

The remainder of this paper is organized as follows. Section 2 reviews prior work on publicly available brain hemorrhage CT datasets and their limitations alongside with some AI-based methodologies for diagnosis of hemorrhage. Section 3 presents the details of our dataset, including its annotation protocols, data composition, and a comparative analysis against existing public datasets. In Section 4, we define the core tasks enabled by our dataset—such as classification, object detection, and segmentation—and describe the baseline models and training protocols used for evaluation. Section 5 reports the experimental results across different tasks and compares model performance to expert annotations. Section 6 discusses the implications of our findings, potential applications, and limitations. Finally, Section 7 concludes the paper with directions for future research.

## 2 Related Works

This section reviews several datasets that have been used in previous research on ICH classification, detection, and segmentation from brain CT scans. These datasets vary in terms of size, annotation detail, public accessibility, and institutional source. Some are fully private, others are publicly available [17, 7, 15, 16], and a few consist of both private and public components [18, 11, 13]. The discussion is divided into two parts: the first part focuses on private and semi-private datasets that are not freely accessible in full; the second part reviews widely used public datasets that support open access for research and benchmarking. For each dataset, the number of CT scans or slices, the inclusion scope, and availability are briefly described. Additionally, recent deep learning approaches applied to different datasets are reviewed to better understand how deep learning methods leverage data sources, laying the groundwork for the methodology section of this study.

## 2.1 Restricted-Access ICH Datasets

Over a ten-year period, a dataset [8] was assembled across thirteen medical centers in the Geisinger Health System in Pennsylvania, USA; comprising 46 583 non-contrast head CT studies—totaling more than 2 000 000 axial slices—and each scan was labeled at the study level through automated extraction from radiology reports. This proprietary resource was employed for both retrospective training and prospective validation of an AI-driven triage system, yet remains inaccessible to external researchers.

Likewise, between 2010 and 2017 a proprietary collection of 4 396 non-contrast head CT scans was amassed from the University of California, San Francisco and its affiliated hospitals, with an additional 200 exams set aside for testing [10]. Pixel-level masks delineating hemorrhagic regions were generated to facilitate both classification and segmentation model development. Despite its value for deep learning experiments in ICH detection and delineation, this dataset remains closed to external access.

Subsequently, two datasets were employed to evaluate segmentation performance in [19]. The first comprised 190 non-contrast head CT scans that were privately collected from patients presenting with acute stroke symptoms, while the second consisted of 75 annotated CT examinations obtained from the publicly accessible PhysioNet [18, 11] repository. Pixel-level masks delineating hemorrhagic regions were provided for both sources, yet external access is granted exclusively to the PhysioNet subset.

Building on these institution-curated collections, a retrospective series of 3 605 consecutive non-contrast head CT studies was acquired from two emergency departments within a single academic medical center [12]. Each scan was independently reviewed by expert neuroradiologists to generate reference-standard labels for benchmarking an AI-driven triage algorithm’s diagnostic accuracy. Although this dataset offers both scale and expert annotation, it remains inaccessible to external researchers.

Transitioning from single-center triage cohorts, a hybrid retrospective–prospective collection was assembled at Xuzhou Central Hospital, encompassing 12 568 non-contrast CT slices from 512 patients in the retrospective arm and 1 257 slices from 50 patients in the prospective arm [13]. Hematoma regions were delineated with pixel-level masks to support both model training and rigorous evaluation. While full access to the raw images remains restricted, a test subset and the accompanying source code have been released for external benchmarking.

Extending the scope to a multi-center framework, CT scans from 1 824 patients imaged between 2018 and 2022 across four tertiary hospitals were pooled to study aneurysmal subarachnoid hemorrhage [14]. Among these, 1 355 cases with confirmed aneurysmal bleeds were selected for detailed segmentation and volumetric analysis. Although the underlying data are not publicly available, this work offers valuable lessons in harmonizing acquisition protocols, annotation guidelines, and preprocessing pipelines across institutions.

More recently, a dataset was curated [20] as part of an initiative within the Moscow healthcare system. A total of 800 non-contrast brain CT scans were selected from diagnostic reports dated between 2020 and 2023, derived from a pool of over 230 000 studies stored in the Unified Radiological Information Service. The dataset includes patient-level classification labels indicating the presence or absence of intracranial hemorrhage and its subtypes as well as associated findings such as skull fractures and break in the cerebrospinal fluid spaces. Each scan was verified by expert radiologists, and technical imaging parameters were documented for every case. Although designed to support both classification research in hemorrhage diagnosis, the dataset was not yet publicly released at the time of writing.

## 2.2 Open-Access ICH Datasets

### 2.2.1 PHE-SICH-CT-IDS

PHE-SICH-CT-IDS [17] is a dataset centred on peri-haematomal oedema generated from spontaneous basal-ganglia hemorrhage; it comprises 3511 axial slices from 120 CT scans of adult patients imaged at Shengjing Hospital of China Medical University in Shenyang, China, using a PHILIPS Brilliance iCT scanner operated at 120 kV. Pixel-level masks are supplied exclusively for the oedema, while hemorrhage regions are delineated with bounding boxes, and the annotators did not assign hemorrhage subtypes. The dataset includes adults who sustained a spontaneous intracerebral hemorrhage limited to the basal ganglia, were imaged with a non-contrast CT scan within 12 hours of symptom onset, underwent no neurosurgical intervention after admission, and repeated the scan within 72 hours. Cases were excluded when image quality was inadequate, a prior neurosurgical procedure had been performed, a coagulation disorder or anticoagulant therapy was present, or the bleed was secondary in origin or extended into the ventricular system.

## 2.2.2 CQ500

Chilamkurthy et al. [7] have published the CQ500 dataset, which was curated as part of a broader effort to develop and validate deep learning algorithms for the detection of critical findings in head CT scans. It serves as an external validation subset drawn from the larger Qure25k dataset, which itself was sourced from multiple medical centers across India using a variety of CT scanner models with 16 to 128 slices per rotation. The CQ500 collection consists of 491 non-contrast head CT scans annotated at the patient level for classification tasks involving five types of intracranial hemorrhage, as well as calvarial fractures, midline shift, and mass effect. This dataset was constructed in two batches; the first batch included all head CT scans performed over a 30-day window starting on November 2017, at selected centers in New Delhi. The second batch was compiled by first applying a rule-based natural language processing (NLP) algorithm to clinical radiology reports to identify cases with specific subtypes of hemorrhage and fractures, followed by stratified random sampling. Both batches excluded patients younger than 7 years, scans with postoperative changes, and series lacking a complete non-contrast axial sequence. The selection process used clinical histories embedded in radiology reports to enrich the data set with relevant pathological findings.

To extend the utility of CQ500 for localization tasks, Reis et al. [21] subsequently introduced the Brain Hemorrhage Extended (BHx) dataset, providing bounding box annotations for five acute hemorrhage subtypes. This enhancement was achieved by manually labeling thick-slice images and extrapolating the results to thin-slice series, resulting in over 39,000 bounding boxes linked to the CQ500 scans. Notably, the CQ500 dataset includes multiple CT scans per patient and provides only patient-wise annotations, which together limit its suitability for certain slice-wise analyses due to potential redundancy, label ambiguity, and non-independence of slices.

To enable pixel-level localization on CQ500, Spahr et al. released Seg-CQ500[22], a public set of binary segmentation masks manually drawn on a subset of CQ500 by two radiologists. In total, the proposed subset contains 51 CT studies with 11,175 slices. Although this segmented subset furthers the utility of CQ500, its limited number of patients and its binary annotations still restrict the capability of developing and benchmarking models for multi-class hemorrhage segmentation or more comprehensive lesion characterization.

## 2.2.3 PhysioNet CT-ICH dataset

Hssayeni et al. [18, 11] introduced a publicly available dataset comprising 75 non-contrast head CT scans with <slice number> slices acquired from Al Hilla Teaching Hospital in Babil, Iraq, using a Siemens SOMATOM Definition AS scanner with 100 kV tube voltage, 5 mm slice thickness, and isotropic resolution of 0.33 mm. The dataset includes pixel-wise semantic segmentation masks for binary hemorrhage delineation, created through a joint consensus by two radiologists who segmented the images together in a non-blinded setting. Only subjects with traumatic brain injury and radiologically confirmed intracranial hemorrhage were included. The dataset specifically encompasses cases exhibiting IPH, IVH, SAH, SDH, and EPH hemorrhages. One subject with a chronic hemorrhage was excluded from the final release. Additionally, 7 patients' CT scans and annotations were missed in the final release. Additionally, the dataset does not contain cases lacking full non-contrast axial brain coverage. Beyond the segmentation masks, the dataset provides patient-wise and slice-wise classification labels in which hemorrhage subtypes are identified. However, the segmentation masks remain binary and do not specify subtypes. Despite its limited size, this dataset offers one of the few open-access resources with full-volume annotations suitable for training and evaluating hemorrhage classification and segmentation tasks.

## 2.2.4 RSNA 2019 Brain CT Hemorrhage Challenge

The Radiological Society of North America (RSNA) 2019 Brain CT Hemorrhage Challenge dataset comprises 25 312 CT scan examinations with 874 035 slices acquired from three institutions across North and South America: Thomas Jefferson University Hospital (USA), Stanford University (USA), and Universidade Federal de São Paulo (Brazil), in collaboration with the American Society of Neuroradiology (ASNR) [15, 16]. Each institution employed distinct case retrieval strategies tailored to its local clinical archive, including using NLP on radiology reports, retrospective sampling of a one-year imaging period, or stratified extraction based on report-derived abnormality findings. The resulting dataset spans a broad range of clinical contexts, including both inpatient and emergency settings, and incorporates imaging acquired on CT scanners from multiple manufacturers. Annotations were conducted over a three-month period by 60 annotators from multiple countries, including both junior and senior ASNR members. Annotators were onboarded with structured training, annotation guidelines, and practice cases prior to dataset review. Each training case was annotated by a single rater, whereas validation and test cases were triple-read; disagreements were adjudicated by senior neuroradiologists. Annotators assigned image-level labels for five hemorrhage subtypes—namely ICH, IVH, SAH, SDH, and EPH—or applied one of two exam-level flags for either normal or non-hemorrhagic abnormal studies. A distinctive feature of the annotation protocol was the option to label only the first and last slices of a hemorrhagic region, with the annotation tool interpolating labels across intervening slices. While this approach expedited the labeling

process, it introduced potential spatial imprecision in hemorrhage localization. Moreover, annotators operated without access to clinical history or demographic data. The most common annotation error identified during auditing was under-labeling, which was addressed in the final release. In contrast, over-labeling and subtype misclassification were acknowledged as natural consequences of inter-reader variability and were not addressed by retraining or correction during the annotation phase. Given the large number of annotators, unresolved variability in over-labeling and subtype classification may contribute to residual uncertainty in the consistency and reliability of the image-level annotations. Notably, this dataset does not include segmentation masks; however, in [23], the authors provided binary segmentation annotations for 192 CT scans, offering a valuable resource for voxel-level hemorrhage detection studies.

Table 1: Summary of public CT hemorrhage datasets.

Dataset	Year	Studies	Number of slices	Annotation type
PHE-SICH-CT-IDS [17]	2024	120 Patients	7 022	CLS, SEG, DET
CQ500 [7]	2018	491 Patients	multiple	Patient-wise CLS
PhysioNet CT-ICH [11]	2020	82 Patients	2 491	SEG, CLS
RSNA [16]	2020	25 312 Patients	874 035	CLS
Hemorica	2025	372 Patients	12 067	CLS, DET, SEG, QUANTIFICATION

Public datasets are shown along with their key characteristics, including slice-wise classification (CLS), detection (DET), segmentation (SEG), patient-wise classification, and volume measurement (QUANTIFICATION) annotations. The term “multiple” indicates that the number of CT scans varies across patients and the number of slices is not uniformly specified.

As summarized in Table 1, current public CT hemorrhage datasets vary in size, scope, and annotation, offering support for a range of AI-related tasks. The PHE-SICH-CT-IDS dataset provides slice-level classification, pixel-wise segmentation, and object-level detection annotations. The original CQ500 includes patient-wise classification labels, although it lacks segmentation or bounding box annotations. PhysioNet CT-ICH offers a smaller sample size but includes both segmentation masks and slice-classification labels, making it suitable for evaluating basic models. The original RSNA 2019 dataset remains the largest publicly available resource in terms of scan volume, with annotations provided for slice-wise and patient-wise classification; however, its annotation protocol involved interpolated labels and minimal quality control, potentially impacting annotation reliability. In contrast, Hemorica has been designed to support a wide range of tasks by including comprehensive annotations for classification, detection, segmentation, and volumetric quantification. It has been collected with attention to annotation accuracy and diversity, allowing for broader applicability in training and evaluating advanced hemorrhage analysis models.

### 2.3 Deep Learning Approaches

Deep learning has been extensively applied to classify and detect intracranial hemorrhages (ICH) on head CT scans, achieving near-radiologist-level accuracy in both ICH presence and subtype identification [7, 10]. Retrospective studies using large datasets and 2D CNNs report high detection accuracy [7], while 3D CNNs have also reached expert-level performance in localizing acute hemorrhages [10]. Beyond binary classification, algorithms now reliably distinguish among hemorrhage subtypes [7]. Weakly supervised methods utilize radiology reports to detect various head CT abnormalities, including hemorrhages, without requiring pixel-level labels. Prospective multicenter validations confirm the generalizability and robustness of these systems across institutions [24]. Targeted models have been developed for specific hemorrhage types, such as subarachnoid hemorrhage [25] and subdural hematomas [26, 24], achieving strong performance. On the segmentation side, numerous studies focus on automating hematoma volume estimation, a key prognostic factor in ICH [27, 28]. U-Net-based architectures have demonstrated accurate segmentation results closely matching manual annotations [27], with automated volume measurements agreeing well with clinical standards like the ABC/2 method [29]. Some models also segment perihematomal edema for a more complete injury assessment [28]. Segmentation performance has improved with architectural innovations, such as 3D U-Nets incorporating squeeze-and-excitation blocks [30]. Many models report Dice similarity coefficients exceeding 0.8, indicating high concordance with expert segmentations [31]. Multi-class segmentation has enabled concurrent labeling of different hemorrhage types and associated edema [32], providing detailed volumetric data critical for decision-making [31]. Techniques like masked loss functions help handle class imbalance and anatomical constraints [33], while prior knowledge (e.g., brain symmetry) enhances model generalization when data is limited [34]. Integrated approaches now combine tasks—such as 2D segmentation followed by subtype classification and volume quantification—within a single pipeline [35]. End-to-end models that detect ICH and produce pixelwise segmentations have also been proposed [36], supporting comprehensive analysis. In traumatic brain injury, deep learning is applied to identify and quantify multiple lesion types (e.g., contusions, subdural, epidural hematomas) for holistic assessment [35]. Several deep learning tools have

undergone clinical validation. FDA-cleared systems for ICH detection maintain high sensitivity and specificity in real-world settings [37], while independent evaluations show that AI models can function as second readers to improve diagnostic confidence without significantly increasing false positives [12]. These tools enhance emergency triage by rapidly flagging hemorrhages and generating objective volume measurements for stroke and trauma care [38]. Given the prognostic importance of hemorrhage volume [28], accurate and reproducible measurement via AI is especially valuable. Rapid, automated ICH classification on CT is crucial in time-sensitive scenarios. Deep learning systems ensure timely detection and alerting of critical cases [7, 8]. Research across classification, detection, and segmentation reflects the complementary nature of these tasks—classification and detection aid triage and diagnosis, while segmentation provides detailed quantitative data [31]. Table 2 presents a summary table of several studies discussed in this paper, highlighting the significant diversity in the methodologies employed. By employing these techniques, deep learning models can together offer a comprehensive AI-assisted solution – flagging the presence of hemorrhage, characterizing its type, and measuring its extent – which has significant potential to improve patient outcomes and streamline acute neuroimaging workflows. Given the increasing focus on such advancements, a comprehensive public dataset can play a pivotal role in supporting the fundamental needs for research and development in this field. Therefore, we believe that to thoroughly evaluate an ICH dataset, it is essential to assess the performance of classification, segmentation, and detection models when trained or fine-tuned on the dataset. This study proposes a understanding of Hemorica's characteristics, capabilities, and limitations across different model types and tasks.

Table 2: Summary of deep learning models used for different tasks in this field.

Literature	Year	Model/Design
[39]	2018	Hybrid 3D/2D CNN
[40]	2019	2D CNN + explainability
[41]	2022	CNN+RNN with attention
[24]	2022	Weakly-supervised CNN
[38]	2021	Hybrid 2D-3D CNN
[37]	2021	CNN (commercial AI)
[42]	2021	CNN (Aidoc)
[27]	2019	3D U-Net (patch-based)
[29]	2019	Custom ML algorithm
[43]	2020	CNN-DS (deep supervision)
[28]	2020	2D U-Net
[30]	2021	3D U-Net + SE blocks
[44]	2022	2D U-Net (robust)
[31]	2022	3D U-Net
[36]	2022	3D CNN (Brainomix)
[35]	2022	Two-stage (seg+cls)
[33]	2023	U-Net + masked loss

### 3 Materials

#### 3.1 Dataset

Hemorica comprises 372 head CT scans, each with 12 068 acquired from the Radiography Center at Rasoul Akram Hospital in Iran. as illustrated in Figure 2, a retrospective review of examinations conducted between 2012 and 2024 was performed, during which an initial set of 420 CT studies was collected. Of these, 48 scans were excluded due to noise, low-quality scans, post-operative radiography, and corrupted files. The remaining 372 CT volumes were exported in Digital Imaging and Communications in Medicine (DICOM) format, converted to Neuroimaging Informatics Technology Initiative (NIFTI) files, and subsequently anonymized to remove all personally identifying information. The CT scan module was

Based on clinical relevance and diagnostic importance, the identification of hemorrhage subtypes is considered a key factor in both treatment planning and clinical outcomes. Accordingly, EPH, SDH, SAH, IPH, and IVH hemorrhages were selected as the target lesion types for detection in CT scan images. For data collection, specific keywords such as "intracranial hemorrhage" and "CT scan," along with exclusion criteria—including postoperative CT scans,

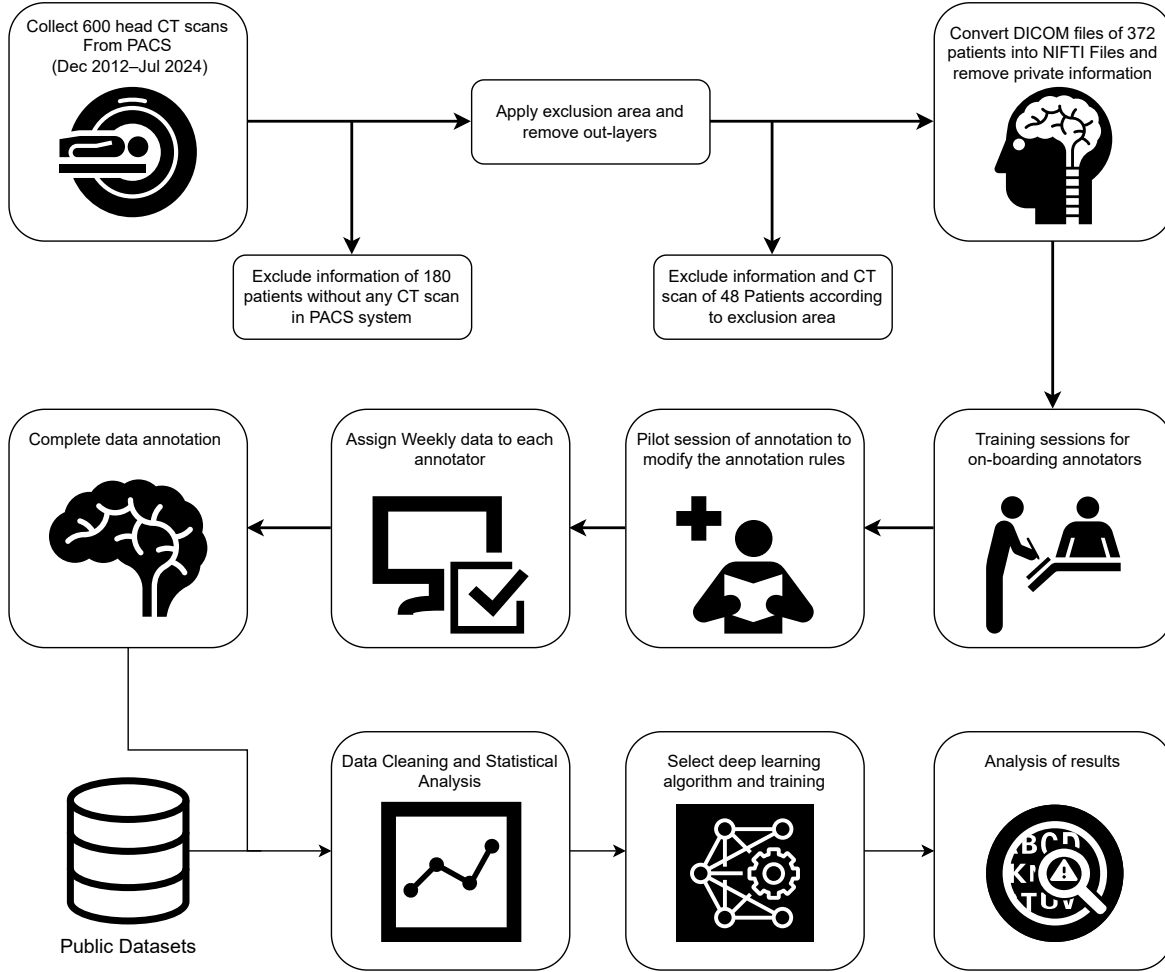


Figure 2: Workflow of data gathering and data annotation. The diagram outlines the multi-phase process of dataset preparation.

low-quality images, and motion artifacts—were used to filter eligible patient records within the Picture Archiving and Communication System (PACS) of Rasoul Akram Hospital. The resulting dataset was subsequently annotated manually to identify instances of the selected hemorrhage subtypes.

The annotation process of hemorrhagic lesions in CT scans was performed using 3D Slicer [45, 46] on local workstations. Since the criteria to identify hemorrhage and the boundary of lesions might differ between two experts, a standardized annotation protocol was developed to delineate five hemorrhagic lesion types and their characteristics to minimize the interclass correlation of annotations between different experts. Training for the annotation team comprised a neurosurgeon who led orientation sessions for both a radiology specialist and a practitioner. The annotation process was conducted manually under full supervision. The radiology specialist and the practitioner were blinded to one another’s work and had no involvement in patient care. Initially, a pilot set of 50 CT scans was annotated independently by both experts; these results were reviewed by the neurosurgeon to establish consensus guidelines and to define rules for borderline cases, thereby minimizing inter-rater variability. Thereafter, weekly annotation batches were distributed, each containing new cases as well as a subset from previous weeks to facilitate ongoing intra- and inter-rater reliability assessment. Annotators had access solely to the CT images, with no additional clinical or historical data provided.

During annotation sessions, the full volumetric CT series was made available in the software interface to preserve spatial context. The Hounsfield Units of each CT volume were processed using a standard brain-window setting, although annotators were permitted to apply custom window level and window width adjustments as needed. For each scan, annotators completed a structured form documenting patient-level labels and supplementary diagnostic observations. To

mitigate fatigue effects, annotation sessions were limited to four to five hours in duration. Ultimately, the radiologist’s annotations were designated as the ground truth for segmentation purposes. The practitioner’s annotations were utilized to evaluate the quality of the ground truth and to compare the segmentation performance and diagnostic accuracy between the two medical experts.

Representative examples of these manual segmentations are shown in Figure 3. Sub-figures (a)–(f) illustrate single-label cases—including healthy control and each of the five hemorrhage subtypes—while panels (g)–(i) display multi-label slices with co-occurring lesions. These overlays demonstrate both the consistency of our annotation protocol across lesion types and the diversity of spatial patterns captured in the dataset.

As a result of the detailed annotation of various hemorrhage subtypes in Hemorica, segmentation masks suitable for identifying hemorrhagic lesions and their respective subclasses were produced. Additionally, by applying connected component algorithms to the subclass masks, corresponding polygons were generated for each hemorrhagic lesion within the CT scan images. These polygonal outlines were subsequently used to derive bounding boxes for each lesion. Furthermore, classification labels were generated to support both patient-wise and slice-wise classification tasks. A standardized protocol for the diagnosis and annotation of CT radiographs was also established, ensuring alignment with established medical conventions.

### 3.2 Dataset and Annotation Statistics

To provide a detailed insight into our dataset, a comprehensive statistical analysis was conducted to encompass different characteristics of the annotated dataset, including the distribution of slices, the distribution of hemorrhagic patients and slices, the distribution of lesion area, and voxel intensity profiles. The results of this analysis are presented through a series of visualizations, as detailed in the subsequent sections.

### 3.3 Slice Distribution

The number of axial slices per CT scan varies significantly across publicly available hemorrhage datasets, largely due to differences in scanner protocols, acquisition settings, and institutional practices. Figure 4 presents histograms comparing the slice distribution in four representative datasets. Hemorica exhibits a slice count ranging from 16 to 56 slices per patient, with a mean of 32.2 and a standard deviation of 7.4. These values are closely aligned with those of the RSNA dataset, indicating similar acquisition profiles. In contrast, the Iraqi dataset shows a higher average number of slices with a tighter spread, while the PHE dataset contains scans with a slightly lower average but a comparable standard deviation. The CQ500 dataset, however, comprises multiple CT scans per patient, each with potentially different slice counts. As a result, the overall slice distribution is not directly available or comparable in a consistent manner. These comparisons suggest that our dataset maintains consistency with widely used benchmarks like RSNA while covering a similar range of anatomical coverage per scan, which is important for ensuring compatibility in downstream training and evaluation scenarios.

### 3.4 Patient-wise Distribution

The patient-wise distribution refers to the analysis of CT scan data at the individual level, where each scan represents a complete diagnostic instance. This approach is maintained to ensure that statistical evaluations reflect realistic clinical scenarios encountered in medical practice. The distribution of healthy and hemorrhagic cases per patient, along with the prevalence of hemorrhage subtypes, has been analyzed across five major datasets containing information to obtain the presence of hemorrhagic lesions and their subtypes in each CT scan. These datasets include Hemorica, PhysioNet CT-ICH, CQ500, PHE-SICH-CT-IDS, and RSNA. It should be noted that the PHE-SICH-CT-IDS dataset provides only a binary indicator of hemorrhage presence per patient, without subtype-level annotations.

As illustrated in Figure 5a, a total of 263 hemorrhagic scans (70.7%) and 109 healthy scans (29.3%) were included in the Hemorica. This distribution closely aligns with those reported in the RSNA dataset (59.2% hemorrhagic, 40.8% healthy) and CQ500 (58.2% hemorrhagic, 41.8% healthy). In contrast, a slightly higher proportion of healthy cases (52% hemorrhagic, 48% healthy) has been observed in the PhysioNet CT-ICH dataset. It is important to note that the PHE-SICH-CT-IDS dataset includes only patients with ICH lesions, and no healthy instances are present.

As it illustrated in Figure 5b, IPH was identified as the most prevalent category in the Hemorica dataset (57.3%), followed by IVH (15.1%), SAH (15.6%), SDH (8.2%), and EPH (3.8%). While IPH was also the most common subtype in the CQ500 (46.5%) and RSNA (31.1%) datasets, the subtype distributions in those datasets differ slightly from distribution of subtypes in the Hemorica dataset. This variation may be attributed to the fact that both CQ500 and RSNA were collected from multiple centers and involved selection processes that included filtering patients by subtype during data acquisition. In these datasets, SAH and SDH were reported at 18.4% and 20.8% in CQ500, and 22.3%

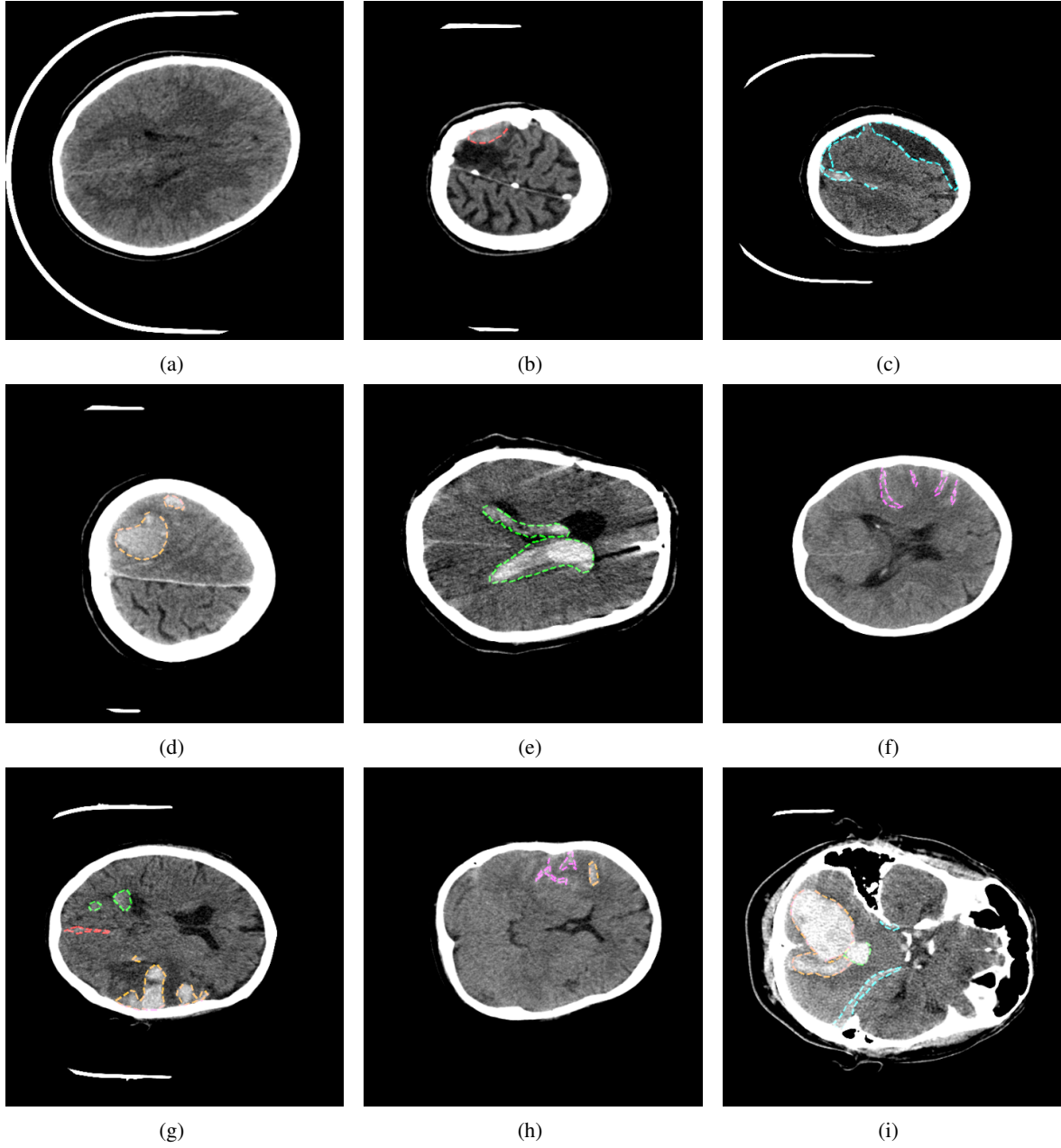


Figure 3: Representative CT slices overlaid with manual segmentations. Each panel displays an axial CT slice annotated with color-coded hemorrhage subtypes: red for EPH, light blue for SDH, orange for IPH, green for IVH, and pink for SAH. Panels illustrate: (a) a healthy slice; (b) EPH; (c) SDH; (d) IPH; (e) IVH; (f) SAH; (g) IVH + EPH + IPH; (h) SAH + IPH; and (i) IPH + SDH.

and 23.0% in RSNA, respectively—substantially higher than the corresponding proportions in the Hemorica dataset. IVH in Hemorica is 15.1% which is between the distribution of RSNA and CQ500. EPH remained rare across all datasets, with reported frequencies of 4.5% in CQ500, 2.1% in RSNA, and 3.8% in the Hamorica dataset. A markedly different subtype distribution was observed in the PhysioNet CT-ICH dataset, where EPH was most prevalent (39.6%), followed by IPH (30.2%), SDH (13.2%), IVH (13.2%), and SAH (7.5%). This deviation indicates that a distinct data collection strategy or clinical inclusion criterion may have been applied. Despite variations across datasets, the distribution of hemorrhage subtypes in Hemorica is consistent with patterns commonly observed in tertiary care settings. This alignment reflects the real-world distribution at the center where the data were collected, supporting the clinical relevance of the dataset and its suitability for developing and evaluating diagnostic models.

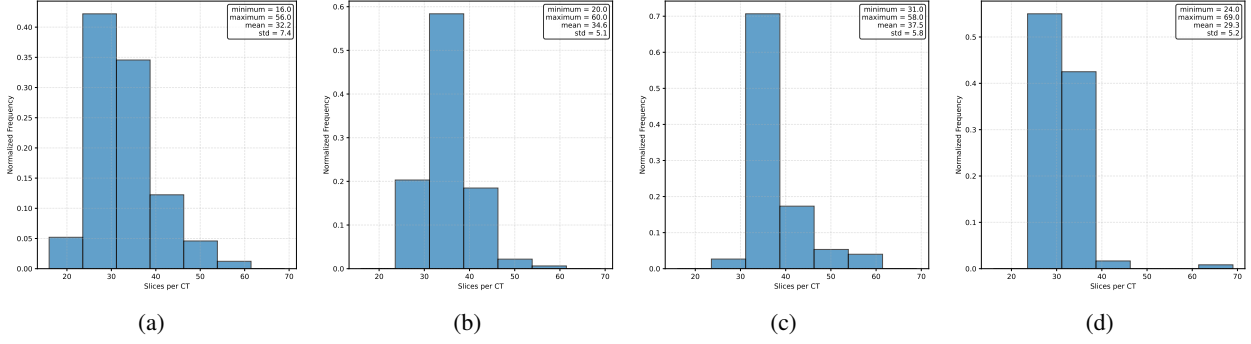


Figure 4: Histograms depicting the distribution of the number of slices per CT scan across four datasets: (a) Hemorica, (b) RSNA, (c) PhysioNet CT-ICH, and (d) PHE-SICH-CT-IDS.

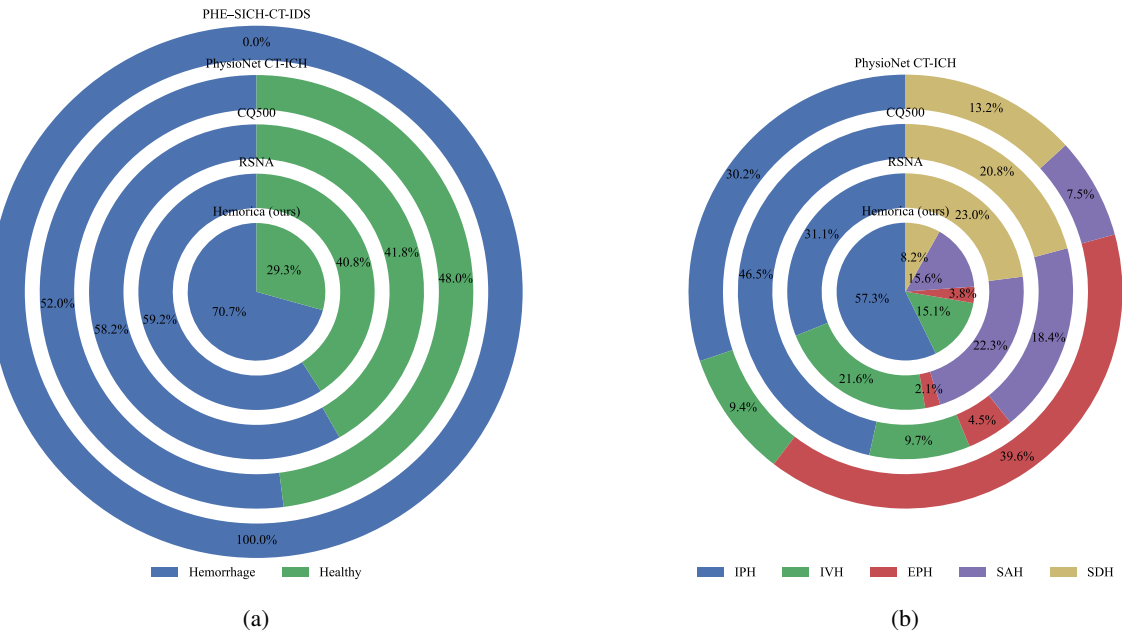


Figure 5: (a) The percentage of healthy cases and patients has been compared on a patient-wise basis between the Hemorica dataset and other publicly available datasets. (b) The distribution of hemorrhage subtypes across these datasets has been presented on a patient-wise basis. The PHE-SICH-CT-IDS does not provide sufficient information to determine the distribution of subtypes of Hemorrhage.

### 3.5 Slice-wise Distribution

A slice-wise analysis was performed to quantify the distribution of hemorrhagic lesions across individual CT scan slices. This level of analysis is critical for developing and evaluating computational models that operate on a per-slice basis.

The binary distributions of healthy and hemorrhagic slices in the Hemorica dataset and other publicly available datasets are illustrated in Figure 6a. In Hemorica dataset, a total of 2,678 (22.2%) hemorrhagic slices and 9,388 (77.8%) healthy slices are identified, which reveals a distinct distribution pattern compared to the patient-wise distribution. Similar trends were observed in RSNA (14.3% hemorrhagic slices), PhysioNet-ICH (11.3% hemorrhagic slices), and PHE-SICH-CT-IDS (20.6% hemorrhagic slices). It is important to note that CQ500 lacks slice-wise annotations, thus it was not included in this comparison.

The slice-wise distribution of hemorrhage subtypes is shown separately in Figure 6b. In Hemorica, among hemorrhagic slices, IPH accounted for 49.7%, IVH for 14.5%, SAH for 23.1%, SDH for 7.8%, and EPH for 4.8%. Comparatively, RSNA showed IPH at 24.4%, IVH at 17.7%, SAH at 31.8%, SDH at 24.1%, and EPH at 2.1%, while PhysioNet-ICH exhibited a fundamentally different distribution with EPH predominant at 50.3%, followed by IPH (21.2%), SAH

(16.3%), SDH (5.2%), and IVH (7.0%). Additionally, it is worth mentioning that the PHE-SICH-CT-IDS dataset does not provide annotations for hemorrhage subtypes. The observed slice-wise distribution closely mirrors the underlying patient-wise diagnoses, as the presence and extent of hemorrhagic lesions across slices inherently reflect patient-level clinical conditions.



Figure 6: (a) The percentage of healthy cases and patients has been compared on a slice-wise basis between the Hemorica dataset and other publicly available datasets. (b) The distribution of hemorrhage subtypes across these datasets has been shown on a slice-wise basis. The original CQ500 does not provide the slice-wise annotation, also PHE-SICH-CT-IDS does not contain information about the subtypes of hemorrhage for CT scans.

### 3.6 Hemorrhage Frequency per-slice

Figure 7 represents the histogram of hemorrhage frequency across different slice numbers. The minimum number of slices containing hemorrhagic lesions is 0, while the maximum number is 42. The most frequent hemorrhage occurrence is observed in the 14th slice of the radiography images while this distribution follows the normal distribution pattern with the mean value of 15.29 and standard deviation of 6.16.

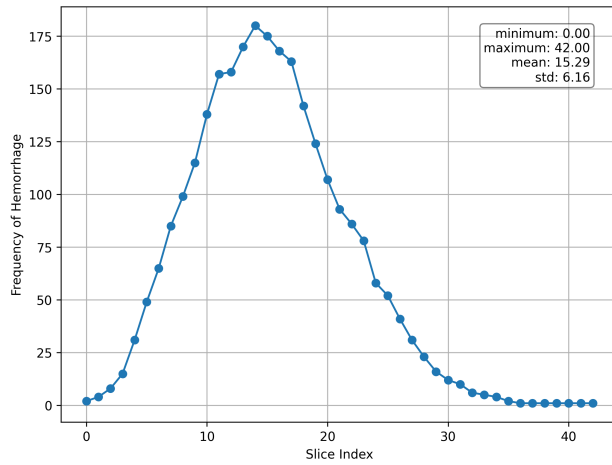


Figure 7: Histogram showing frequency of hemorrhage per slice number.

### 3.7 Lesion Area Distribution

To analyze the spatial extent of hemorrhagic lesions, the distribution of lesion areas per slice was examined across multiple datasets. These analyses provide insights into the morphological variability of annotations and help assess the quality of labels used for training segmentation and detection models.

Figure 8 illustrates the distribution of lesion areas for different hemorrhage subtypes in the Hemorica. It can be observed that IPH lesions exhibit the widest range and largest median area, with a maximum of 27 322 voxels in one slice and a median of 1 985, and mean of 3 076. In contrast, IVH and SAH lesions are the smallest in both mean, median, and range that suggests challenging morphology for identification of these subtypes. These differences highlight the heterogeneity of hemorrhage patterns across subtypes and the importance of subtype-specific modeling.

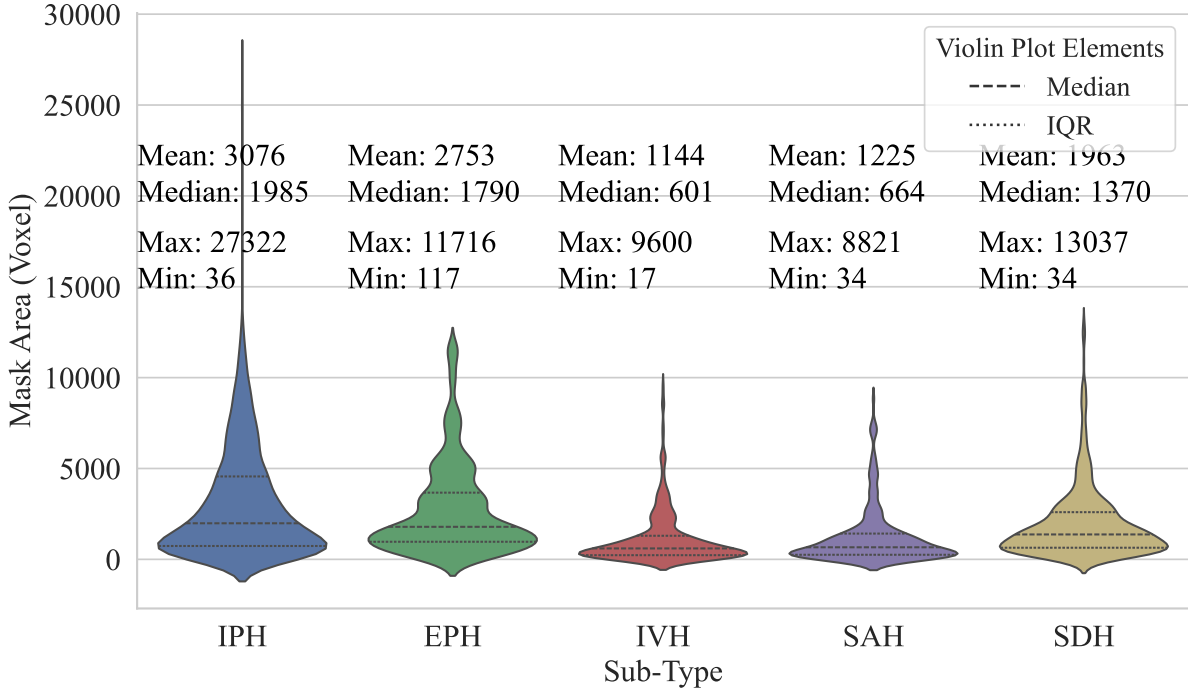


Figure 8: Distribution of lesion areas (in voxels) for different hemorrhage subtypes in the Hemorica dataset. The violin plots show the distribution of lesion sizes for IPH, EPH, IVH, SAH, and SDH, with statistical annotations for mean, median, min, and max values. The dashed lines indicate the median, and the dotted lines represent the interquartile range (IQR). The plot highlights that IPH lesions are larger and more variable, while EPH lesions are smaller and more concentrated.

A comparison of lesion area distributions between the Hemorica and other public datasets is shown in Figure 9. In Figure 9a, the bounding box areas between the Hemorica dataset and the PHE-SICH-CT-IDS dataset are compared. Since the PHE-SICH-CT-IDS dataset does not provide any information about hemorrhage subtypes, this comparison is limited to binary detection of hemorrhagic presence. The Hemorica exhibits a mean bounding box area of 3 172 voxels, which is substantially smaller than the mean of 9 862 voxels observed in the PHE-SICH-CT-IDS dataset. This difference may be attributed not only to variations in annotation protocols—wherein the PHE-SICH-CT-IDS dataset may have employed larger or more inclusive bounding boxes—but also to differences in data collection strategies. Specifically, in PHE-SICH-CT-IDS, only certain subtypes of hemorrhage may have been selectively gathered, potentially biasing the dataset toward cases with larger or more anatomically extensive lesions.

In contrast, Figure 9b presents a comparison based on segmentation mask areas between the Hemorica and the PhysioNet CT-ICH dataset. The mean lesion area in the Hemorica (2 885 voxels) exceeds that of the PhysioNet dataset (1 949 voxels), indicating that the Hemorica dataset includes hemorrhagic instances with generally larger spatial extent. Despite this difference in average area, the overall distributions in the two datasets appear similar, suggesting that comparable annotation protocols were likely employed. Therefore, the observed variation in mean area may primarily reflect differences in the underlying case compositions rather than systematic differences in labeling practices.

Together, these distributions support the conclusion that the Hemorica dataset presents a representative spectrum of lesion sizes, consistent with realistic diagnostic variation encountered in clinical practice. Such diversity enhances the robustness of models trained on this dataset for both detection and segmentation tasks.

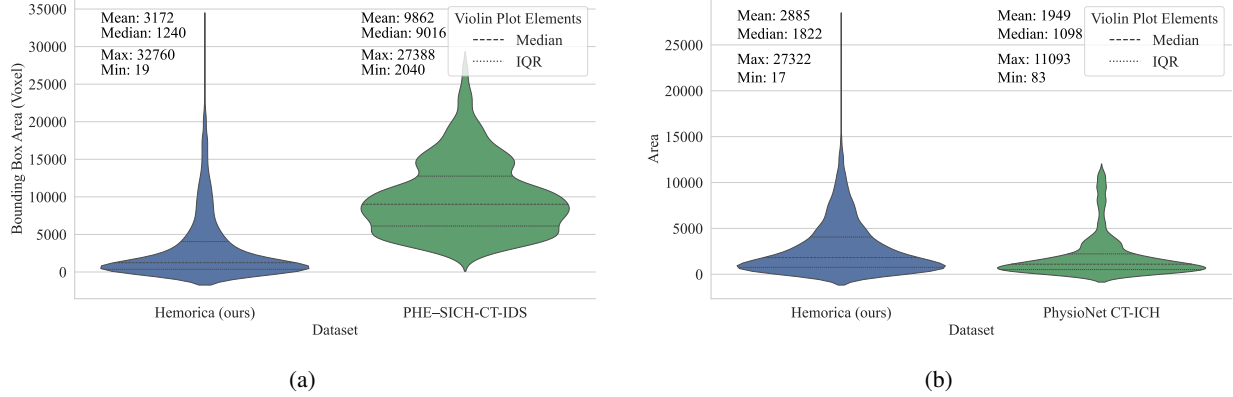


Figure 9: Distributions of lesions in different datasets. The dashed lines indicate the median, and the dotted lines represent the IQR. (a) the area of lesion bounding boxes in our dataset and PHE-SICH-CT-IDS. (b) the area of lesion masks in our dataset and PhysioNet CT-ICH.

### 3.8 Heatmap Localization

A spatial analysis was conducted to examine the anatomical distribution of hemorrhagic lesions across axial slices. A set of heatmaps was generated to facilitate this analysis: a binary aggregation of all lesion regions (Figure 10a), and subtype-specific maps for IPH (Figure 10b), IVH (Figure 10c), EPH (Figure 10d), SDH (Figure 10e), and SAH (Figure 10f). In addition, any-hemorrhage frequency in the training (Figure 10g) and validation (Figure 10h) splits was visualized, and a comparative map from the PhysioNet CT-ICH dataset was included (Figure 10i). Each heatmap was normalized by its modal value to enhance inter-map comparisons, as shown in Figure 10.

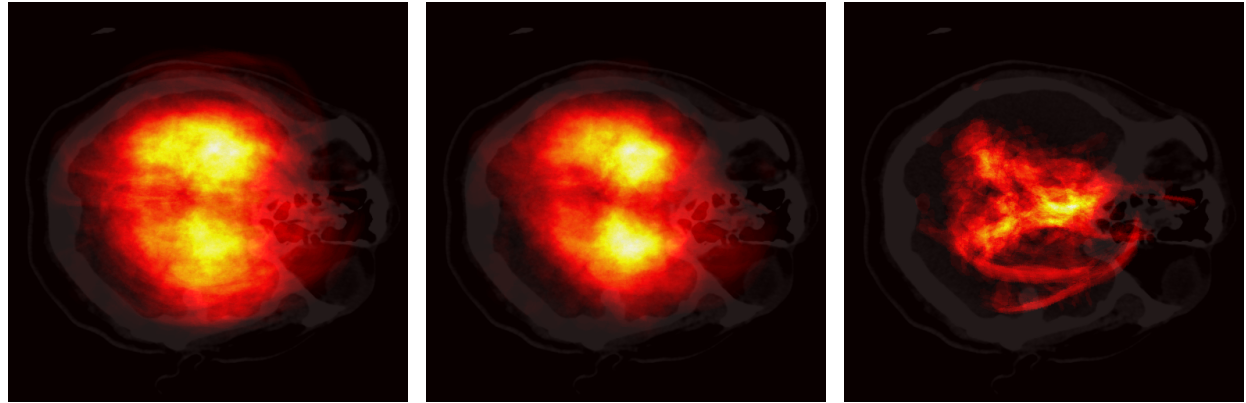
These maps offer critical insight into spatial prevalence: by summing normalized masks across all slices, intensity values reflect hemorrhage occurrence frequency at each voxel location, thereby revealing subtype-specific localization patterns. To ensure anatomical consistency, all CT volumes were preprocessed by correcting head orientation and rotation so that each skull was aligned with the nose pointing horizontally to the right. This alignment reduced inter-patient variability and enabled meaningful spatial aggregation.

The analysis reveals distinct patterns for each subtype. High central activation is observed in the IPH (Figure 10b) and IVH (Figure 10c) maps, indicating deep-parenchymal and intraventricular occurrence. SDH (Figure 10e) and SAH (Figure 10f) maps show elevated intensity along superior and peripheral brain regions adjacent to the inner skull surface, consistent with subdural and subarachnoid localization. From these heatmaps, the morphological characteristics of these subtypes are recognizable and suggest that these subtypes are challenging for AI models. EPH (Figure 10d), though rare, also demonstrates peripheral distribution. Notably, all subtype maps lack significant activation at the extreme lateral boundaries, indicating that hemorrhages seldom occur at the outermost cortical edges.

Compared with the PhysioNet CT-ICH map (Figure 10i), which displays broader and more diffuse lesion localization, the Hemorica maps exhibit tighter spatial coherence—likely reflecting more uniform inclusion criteria and acquisition protocols. Additionally, the similarity between the training (Figure 10g) and validation (Figure 10h) heatmaps indicates that the patient-wise split of the dataset preserves consistent spatial patterns and lesion localization characteristics. This suggests that both subsets represent comparable anatomical distributions, thereby supporting robust model generalization and reducing the risk of distributional bias. Overall, these heatmaps substantiate the anatomical validity of the annotations and provide a valuable reference for both clinical interpretation and the design of location-aware neural architectures.

### 3.9 Intensity Distribution

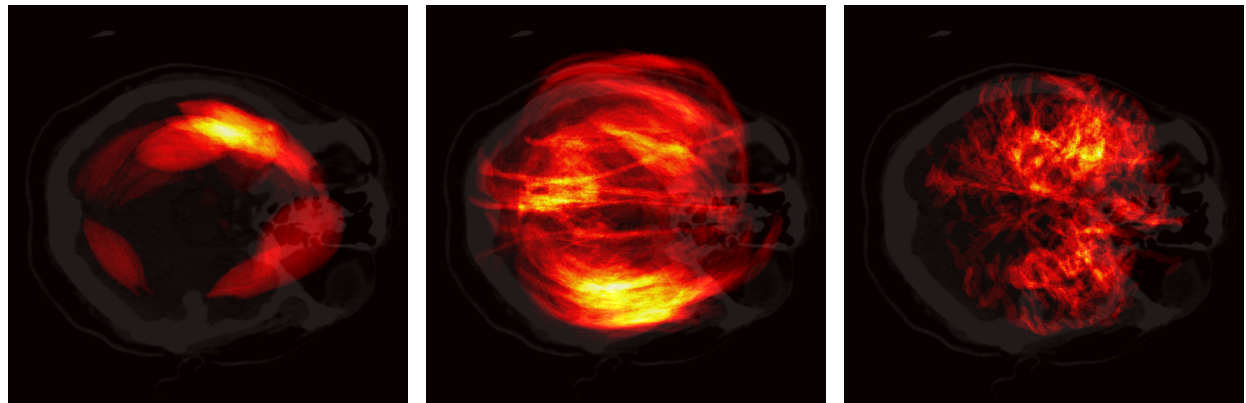
To characterize the intensity properties of hemorrhagic lesions in comparison with normal brain tissue, the distribution of HU values was analyzed for all voxels and for voxels labeled as hemorrhagic. HU values were clipped between  $-50$  and  $100$  to exclude extreme outliers and focus on the typical range of brain tissue intensities. This range was chosen



(a) Binary hemorrhage

(b) IPH

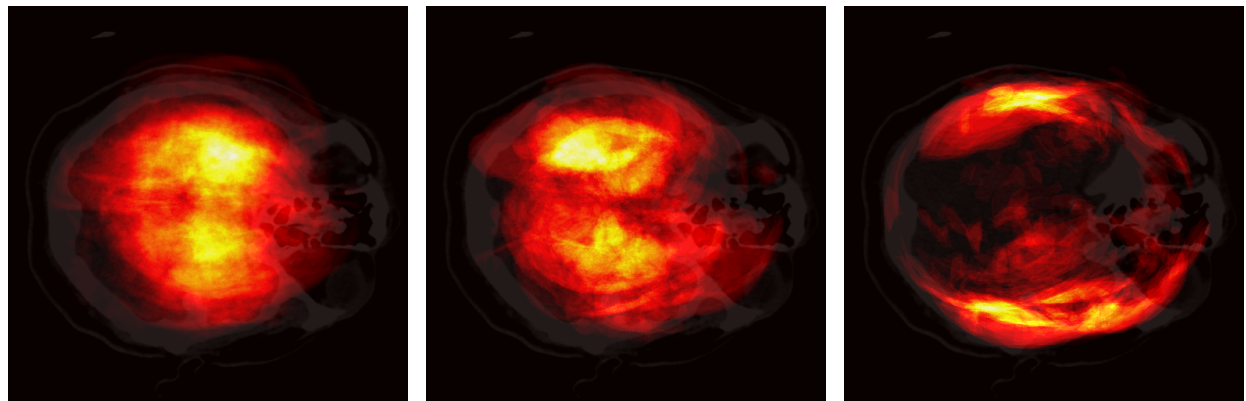
(c) IVH



(d) EPH

(e) SDH

(f) SAH



(g) Training split

(h) Validation split

(i) PhysioNet CT-ICH binary hemorrhage

Figure 10: Heatmaps depicting the frequency of hemorrhage occurrence across different datasets and subtypes. Yellow regions indicate the highest frequency of hemorrhage (by pixel count), while darker regions indicate little to no occurrence. Each map was normalized independently due to subtype imbalance.

because the vast majority of brain voxels fall within these limits, and the histogram reveals that values near  $-50$  and  $100$  occur with negligible frequency.

The resulting normalized distributions are shown in Figure 11. In the Hemorica dataset, hemorrhagic voxels exhibit a distinct unimodal distribution, characterized by a single prominent peak at higher HU values compared to the general brain tissue. This peak appears brighter and denser than the main mode of all brain voxels, indicating a clear separation between hemorrhagic and non-hemorrhagic tissue intensities. The concentrated and elevated HU values suggest that the hemorrhagic regions in the dataset are relatively homogeneous and hyperdense, possibly due to consistent imaging protocols or the prevalence of acute hemorrhage cases. This well-defined distribution enhances the separability of hemorrhagic tissue, which may benefit downstream tasks such as segmentation and classification.

In contrast, the PhysioNet CT-ICH dataset also displays a bimodal distribution for hemorrhagic voxels but with a different intensity profile. One of the peaks aligns with that of the Hemorica dataset, whereas the second appears in a lower HU range—darker than the mean brain voxel intensity. This suggests a difference in data collection or potential variation in annotation or acquisition protocols.

These intensity profiles offer important insights for preprocessing strategies, particularly in determining appropriate windowing settings. They also highlight the relevance of HU-based features for downstream modeling in hemorrhage classification, detection, and segmentation.

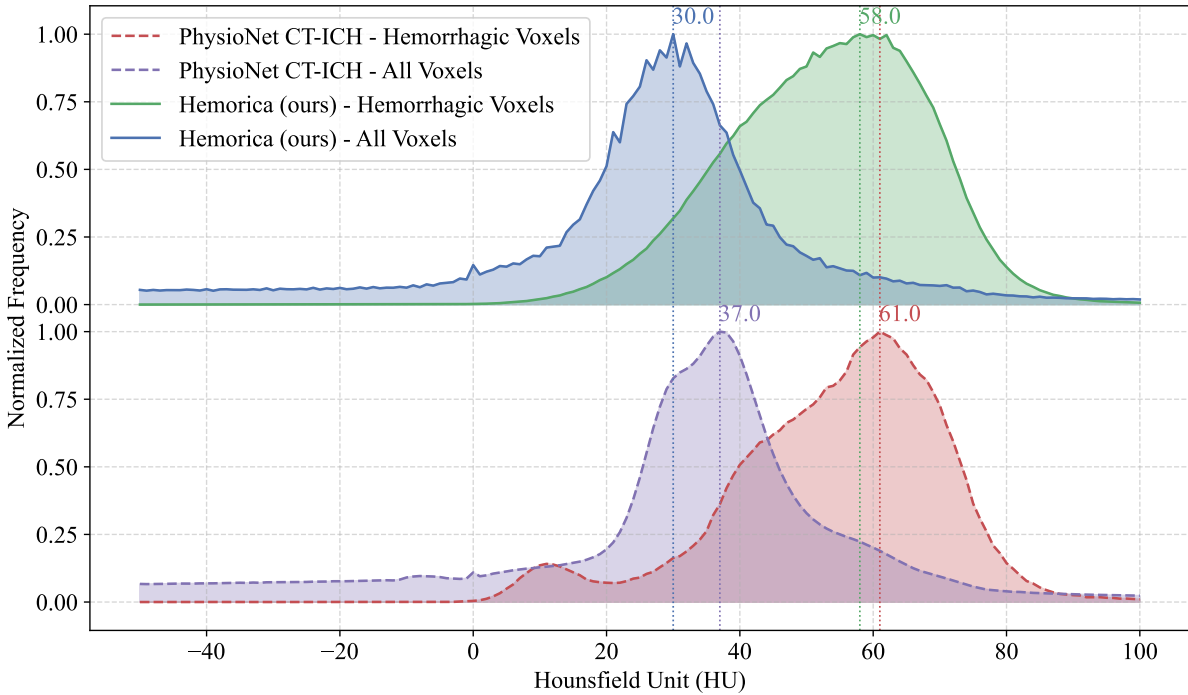


Figure 11: Histogram of Hounsfield Unit (HU) values comparing all voxels in the dataset versus voxels belonging to hemorrhagic lesions.

Conditional probability offers a way to understand how likely one event is to occur, given that another has already occurred. In this context, we use conditional probability to estimate how frequently one subtype of intracranial hemorrhage (e.g., IVH) co-occurs with another subtype (e.g., IPH) within the same patient or slice. This is represented as  $P(m | n)$ , which means “the probability of subtype  $m$  given that subtype  $n$  is present.”

Equation 1 describes the probability of observing event  $m$  given that event  $n$  has occurred, calculated by dividing the probability of both events happening together by the probability of the given event  $n$ .

$$P(m | n) = \frac{P(m \cap n)}{P(n)} \quad (1)$$

Table 3 shows patient-wise conditional probabilities derived from four datasets: Hemorica, RSNA, PhysioNet CT-ICH, and CQ500. In all datasets, IPH appears frequently alongside other hemorrhage types. For example,  $P(\text{IPH} \mid \text{IVH})$  reaches as high as 0.891 in the Hemorica dataset, 0.893 in CQ500, and 0.800 in PhysioNet, and 0.748 in RSNA indicating strong co-occurrence between IPH when the IVH is available across patient records. EPH, in contrast, tends to appear in isolation, with very low co-occurrence values.

The slice-wise conditional probabilities in Table 4 provide a more localized view. As expected, co-occurrence values decrease across most pairs compared to patient-level statistics, reflecting the fact that hemorrhages can appear in different slices of the same scan. Nevertheless, similar trends are preserved. For example, IPH and IVH continue to co-occur frequently, though less strongly. Again, EPH exhibits minimal overlap with other types at the slice level, reinforcing its tendency to occur independently in both spatial and diagnostic dimensions.

These observations suggest that IPH serves as a central and often co-existing subtype in multi-hemorrhage presentations, particularly with IVH. In contrast, EPH is more frequently isolated in both patient-wise and slice-wise distributions. These co-occurrence trends are important for understanding subtype correlation structures, improving multi-label classification performance, and guiding annotation protocols in hemorrhage detection tasks.

Table 3: Patient-wise Conditional Probabilities  $P(m \mid n)$  for Hemorrhage Subtypes where m is the row and n is the column.

Hemorica						RSNA						
	IPH	IVH	EPH	SDH	SAH		IPH	IVH	EPH	SDH	SAH	
IPH	1.000	0.891	0.071	0.404	0.400		IPH	1.000	0.748	0.510	0.446	0.627
IVH	0.234	1.000	0.000	0.193	0.200		IVH	0.528	1.000	0.248	0.296	0.526
EPH	0.005	0.000	1.000	0.035	0.167		EPH	0.034	0.023	1.000	0.045	0.039
SDH	0.110	0.200	0.143	1.000	0.367		SDH	0.322	0.303	0.487	1.000	0.428
SAH	0.057	0.109	0.357	0.193	1.000		SAH	0.463	0.550	0.429	0.438	1.000

PhysioNet CT-ICH						CQ500						
	IPH	IVH	EPH	SDH	SAH		IPH	IVH	EPH	SDH	SAH	
IPH	1.000	0.800	0.191	0.500	0.714		IPH	1.000	0.893	0.539	0.245	0.633
IVH	0.250	1.000	0.048	0.000	0.429		IVH	0.187	1.000	0.077	0.019	0.250
EPH	0.250	0.200	1.000	0.250	0.286		EPH	0.052	0.036	1.000	0.113	0.067
SDH	0.125	0.000	0.048	1.000	0.000		SDH	0.097	0.036	0.462	1.000	0.167
SAH	0.313	0.600	0.095	0.000	1.000		SAH	0.284	0.536	0.308	0.189	1.000

## 4 Methodology

This study investigates the performance of deep learning models on the Hemorica dataset through two main parts. The first part focuses on basic fine-tuning of multiple classification models to evaluate the dataset’s capacity to support effective learning in binary classification. The second part follows the same criteria, focusing on assessing the dataset’s suitability for the binary segmentation.

### 4.1 Classification

In this part, a number of well-established 2D classification models were fine-tuned on the proposed dataset to assess whether it exhibits the characteristics necessary to support effective model training and reliable analysis within the target task. While it is technically possible to perform 3D classification or segmentation with 2D annotations, the scope of this study is limited to 2D models to assess the annotation quality in a slice-wise manner. The list of selected models, which were initialized with pre-trained weights from ImageNet-1k[47], includes ResNet[48] (18, 50), DenseNet[49] (121, 201), EfficientNetV2[50] (small, large), Swin Transformer V2[51] (tiny, small), and MobileViT[52] (XS, S) all of which are widely recognized as strong performers on the ImageNet Benchmark.

This architectural diversity ensures that the baseline examination accounts for different feature extraction strategies, providing a reliable assessment of the dataset’s suitability for the classification task. Furthermore, effective learning

Table 4: Slice-wise Conditional Probabilities  $P(m | n)$  for Hemorrhage Subtypes where m is the row and n is the column.

Hemorica					RSNA							
	IPH	IVH	EPH	SDH	SAH		IPH	IVH	EPH	SDH	SAH	
IPH	1.000	0.578	0.038	0.170	0.241		IPH	1.000	0.401	0.204	0.155	0.257
IVH	0.168	1.000	0.000	0.077	0.079		IVH	0.291	1.000	0.072	0.079	0.212
EPH	0.004	0.000	1.000	0.011	0.067		EPH	0.018	0.009	1.000	0.015	0.016
SDH	0.079	0.123	0.051	1.000	0.202		SDH	0.202	0.143	0.230	1.000	0.262
SAH	0.038	0.043	0.108	0.068	1.000		SAH	0.254	0.289	0.181	0.198	1.000

PhysioNet CT-ICH					
	IPH	IVH	EPH	SDH	SAH
IPH	1.000	0.375	0.023	0.071	0.278
IVH	0.123	1.000	0.000	0.000	0.167
EPH	0.055	0.000	1.000	0.000	0.111
SDH	0.055	0.000	0.000	1.000	0.000
SAH	0.069	0.125	0.012	0.000	1.000

Table 5: Number of Parameters for Selected Models in Binary Classification.

Model Family	Variants	Parameters (M)
ResNet	18 / 50	11.7 / 25.6
DenseNet	121 / 161	7.9 / 26.5
EfficientNet V2	Small / Large	21.5 / 118.5
Swin Transformer V2	Tiny / Small	28.3 / 49.7
MobileViT	XS / S	2.3 / 5.6

using foundational architectures such as ResNet can serve as an indicator of the dataset’s potential to support more complex variants, such as ResNext[53], and SE-ResNext[54]. With respect to the dataset preparation, for all models, input images were normalized to the  $[0, 1]$  range, and resized to 224 x 224 pixels. The Hounsefield Unit (HU) values were limited to the brain window by setting window width to 40 and window length to 80. The input to the models was constructed by concatenating the single-channel grayscale CT scan twice along the channel dimension to create the three-channel input required for the models. In line with the goal of establishing baseline performances, no additional techniques or filters were applied to the input image. The dataset was split into train and test set with a ratio of 0.80, and 0.20, respectively. To avoid data leakage, a patient-wise splitting strategy was employed to keep all slices from a given patient entirely within train or test. Furthermore, both train and test sets were split in a way to similar subtype distributions. To ensure reproducibility, the data split was conducted using a fixed random seed. Table 6 demonstrates the distribution of train and test sets used in the the basic fine-tunings for classification and segmentation tasks. Concerning fine-tuning settings, all models were trained using a consistent set of basic hyperparameters. Cross-Entropy Loss [55] and the Adam [56] optimizer were used as the loss function and optimization algorithm, respectively. The learning rate was set to  $1 \times 10^{-3}$  for convolutional models and  $1 \times 10^{-4}$  for SwinV2 and MobileViT, with no learning rate scheduler applied. For output activation, sigmoid was used in the tasks. For binary classification, model performance was evaluated at a threshold of 0.5 using precision, recall, F1 score, and AUC. Moreover, all experiments were conducted on a system equipped with an NVIDIA GeForce RTX 4070 GPU. The detailed specifications of fine-tuning settings are provided in Table 7, while the results for each specific model, including performance metrics, are presented in the Results section and further analyzed in the Discussion section.

## 4.2 Segmentation

In this part, we aim to achieve a similar objective as in the classification task: Assessing the dataset’s quality for effective learning, and its capability to be used for the segmentation task. Accordingly, the procedures for model selection,

Table 6: Patient-wise and Slice-wise statistics of the data split.

Set	Patients	Patient-wise counts						Slices	Slice-wise counts							
		Healthy	Hemorrhage	IPH	IVH	EPH	SDH		Healthy	Hemorrhage	IPH	IVH	EPH	SDH	SAH	
Train	298	86	212	166	45	11	47	26	9638	7482	2156	1270	380	113	633	232
Test	74	23	51	43	10	3	10	4	2429	1906	523	346	91	44	119	21

preprocessing, data splitting, and fine-tuning configurations follow criteria similar to those used in the classification phase. For the evaluation, two widely segmentation architectures were used: UNet [57] and PSPNet[58]. Both models employ an encoder-decoder architecture. Therefore, to ensure consistency with the classification experiments and to rigorously evaluate Hemorica’s suitability for segmentation, most of the models used in the classification task were reused as encoders of the segmentation models. This approach enables a direct comparison across tasks and provides a cohesive understanding of how well the models perform when fine-tuned on this dataset. Subsequently, the dataset preparation is exactly the same with the classification task and fine-tuning configuration is summarized in Table 7. Detailed results for each specific model, including performance metrics, are presented and discussed in the Results and Discussion sections.

Table 7: Training configuration summary for classification and segmentation tasks.

Parameter	Classification	Segmentation
Pre-trained Weights	ImageNet-1K	ImageNet-1K
Metrics Reported	Precision, Recall, Specificity, $F_1$ score, AUC	Precision, Recall, Dice, IoU
<i>Shared configuration for both tasks:</i>		
Output Activation	Sigmoid	
Input Mode	Grayscale slice replicated to 3 channels	
Windowing	Width = 80, Length = 40	
Image Size	224 × 224	
Batch Size	16	
Epochs	50	
Loss Function	Cross Entropy Loss	
Optimizer	Adam	
Random Seed	32	
Framework	PyTorch	
Device	Nvidia GeForce RTX 4070	

## 5 Results

In this section, the performance of models fine-tuned on the proposed dataset is presented to evaluate whether standard benchmark models can be effectively trained on it. As outlined in the methodology section, all experiments were conducted using similar basic hyperparameters and training settings, ensuring a consistent evaluation of the dataset’s ability to support learning across different deep learning models.

### 5.1 Binary Classification

In this part, the reports of 10 models for binary classification are demonstrated in Table 8. For each model, results were reported as the average across the top 10 epochs with the lowest validation loss. Validation loss was selected as the reference criterion because it directly reflects generalization performance on unseen data, rather than training dynamics alone. To avoid choosing unstable results, only checkpoints after the 10th epoch were considered, because the first 10 epochs often exhibit unstable gradients and rapidly changing weights; therefore, metrics are not yet a reliable representation of model convergence. As shown in the table, all models achieved precision greater than 85.8% and recall greater than 79.6%, indicating effective learning across different architectures. The close F1-score range across different models (83.0%–88.9%) demonstrates similar yet trustworthy performance. MobileViT S and DenseNet 121 achieve the highest F1-score among ViT and CNN architectures, respectively. Across both families, AUCs exceeded

95.9%, highlighting the dataset’s robustness to threshold choice. In addition, joint analysis of Table 5 and Table 8 can guide model selection in further studies. Overall, the competitive scores of selected models indicate that the proposed dataset provides a sufficient amount of informative features for binary classification, achieving an average F1 score of 88.0% for all models with basic fine-tuning.

Table 8: Performance Metrics for Binary Classification.

Model	Precision (%)	Recall (%)	F1 Score (%)	AUC (%)	Specificity (%)
EfficientNetV2 B0	90.5	79.6	84.7	96.6	97.7
EfficientNet V2 Large	90.8	84.6	87.5	97.6	97.6
ResNet 18	85.8	80.7	83.0	95.9	96.2
ResNet 50	87.1	80.4	83.6	96.4	96.7
DenseNet 121	90.5	84.5	87.3	97.5	97.5
DenseNet 161	90.2	84.2	87.0	97.4	97.5
SwinV2 Tiny	92.4	80.9	86.0	97.4	98.1
SwinV2 Small	88.5	83.1	85.5	97.1	96.9
MobileViT XS	89.2	86.6	87.8	97.1	97.1
MobileViT S	91.4	86.7	88.9	97.6	97.7

Furthermore, a recurring pattern in which Recall consistently falls below Precision is a point to an inherent class imbalance in the dataset—a well-known issue in intracranial-hemorrhage collections, where positive samples are under-represented both slice-wise and pixel-wise. This imbalance is particularly consequential in medical diagnosis, where the cost of false negatives generally exceeds that of false positives. Subsequently, further fine-tunings can result in a model with better results.

## 5.2 Binary Segmentation

This part focuses on demonstrating the performance metrics of models for binary segmentation. Table 9 reports Precision, Recall, Dice score, and IoU in a Similar policy to classification part. Across all models, the mean Dice score is 82.3%, a promising result given the minimal fine-tuning and the natural pixel-level class imbalance that makes segmentation inherently more challenging than classification in such dataset. Figure 8 illustrates that the mean mask area for the IPH subtype, the subtype with the most mask area, is under 3100 pixels, which is 6% of the total area in one input image. The effect of this pixel-wise imbalance is evident when comparing the segmentation results in Table 9 to the classification results in Table 8, where the latter demonstrates higher performance across models.

Subsequently, UNet family consistently outperformed PSPNet variants across all encoders. For instance, UNet paired with DenseNet161 achieved a Dice Score of 0.855, while PSPNet with the same encoder achieved 0.808. This trend held true for other encoders, indicating UNet’s superior ability to extract pixel-wise details in binary segmentation tasks. Collectively, comparing Table 8 with Table 9 shows that the mean recall for models dropped by approximately 6.8%. However, the average precision for classification and segmentation results is similar. This suggests that pixel-wise scarcity makes pixel-wise decision-making in the segmentation task more challenging, and this could serve as a signal for fine-tuning policies in future studies. Based on the results, swapping encoders within a given architecture (e.g., UNet) caused smaller performance fluctuations than holding the encoder fixed and changing the overall architecture, indicating that—for this task and training setup—the backbone choice is the primary driver of segmentation accuracy.

## 6 Discussion

ICH is a medical emergency in which timely and precise diagnosis is critical for effective treatment and for reducing the risk of severe disability or death [5]. Rapid diagnosis of ICH and determining its cause are critical for initiating timely treatments such as blood pressure control, reversing anticoagulation, or considering neurosurgical intervention[59]. ICH may arise from traumatic brain injury, cerebrovascular disease, or congenital malformations, and is classified according to the anatomical site and characteristic of bleeding within the cranial vault [6]. Each year, an estimated 40 000–67 000 patients with ICH are identified in the United States, and the 30-day case-fatality rate approaches 40%, making ICH one of the deadliest neurological disorders. In addition to its high risk of death, ICH also causes serious long-term

Table 9: Performance Metrics for Binary Segmentation.

Model	Encoder	Precision(%)	Recall(%)	Dice Score(%)	IoU(%)
UNet	EfficientNet B0	91.7	77.7	84.1	72.5
UNet	EfficientNet B5	91.7	77.4	83.9	72.3
UNet	ResNet 18	90.2	77.8	83.5	71.7
UNet	ResNet 50	90.8	78.5	84.1	72.6
UNet	DenseNet 121	90.5	79.1	84.4	73.0
UNet	DenseNet 161	90.5	81.1	85.5	74.7
UNet	SwinV2 Tiny	88.9	79.1	83.6	71.8
UNet	SwinV2 Small	90.1	78.2	83.7	72.0
PSPNet	EfficientNet B0	87.2	75.7	81.0	68.1
PSPNet	EfficientNet B5	88.2	75.9	81.5	68.8
PSPNet	ResNet 18	88.7	73.4	80.2	67.0
PSPNet	ResNet 50	89.3	74.6	81.2	68.3
PSPNet	DenseNet 121	90.2	74.3	81.5	68.7
PSPNet	DenseNet 161	88.9	74.1	80.8	67.7
PSPNet	SwinV2 Tiny	87.7	72.2	79.2	65.5
PSPNet	SwinV2 Small	88.1	72.0	79.2	65.6

health problems; for example, more than 46% of people who survive certain subtypes suffer permanent cognitive impairment [8]. Given the high mortality and morbidity associated with ICH, rapid and accurate imaging-based diagnosis is essential [10]. CT scan remains the most widely used modality for the prompt detection of acute intracranial bleeding—particularly in emergency settings—because it provides clinicians with the requisite diagnostic accuracy [7, 8, 5].

In terms of fine-grained annotation, Hemorica is the first publicly available dataset with a sufficient number of CT scans that includes comprehensive annotations for multi-class tasks—namely classification, detection, and segmentation—at both the patient-wise and slice-wise levels. This distinguishes Hemorica from existing datasets such as RSNA [15, 16], which does not support detection or segmentation tasks; CQ500 [7], which provides only patient-wise classification labels; PHE-SICH-CT-IDS [17], which includes slice-wise binary classification and detection labels but lacks healthy patients necessary for patient-wise classification; and PhysioNet CT-ICH [18, 11], which does not support multi-class segmentation and lacks detection annotations, in addition to having a limited number of patients.

The inclusion of bounding boxes and segmentation masks for different hemorrhage subtypes in Hemorica offers detailed spatial information, which enables localization-aware training and model explainability—capabilities that are not feasible with classification-only datasets. In addition, the distribution of patients and hemorrhage subtypes in the test set reflects real-world clinical statistics from Rasoul Akram Hospital, without pre-selection of specific subtypes from the PACS system. This real-world representation allows for a more accurate evaluation of model performance in clinical settings. Furthermore, since annotations for classification, detection, and segmentation are all provided, the use of multi-task models and multi-task learning, including sequential and cascaded approaches, is facilitated by the structure of Hemorica. The availability of mask annotations, combined with the substantial number of CT scans and slices, provides a strong foundation for transferring learned models to larger but weakly-labeled datasets (e.g., RSNA), thereby improving sample efficiency in downstream tasks. Additionally, the annotation process was carefully designed to ensure quality and consistency. It involved two blinded annotators and a preliminary pilot phase, with consultation from a neurosurgeon, which helped to minimize inter-rater variability and enhance the reliability of the labels.

As shown in the dataset statistics, the distribution of CT slices in Hemorica closely resembles that of the RSNA dataset, which includes a large number of CT scan samples. This similarity suggests that the slice-level distribution in Hemorica reflects real-world clinical imaging patterns more accurately than datasets with narrower slice distributions. Additionally, the proportion of healthy scans to hemorrhagic scans, as well as the ratio of healthy to hemorrhagic slices, is comparable to those observed in other publicly available datasets. This alignment indicates that the fundamental criteria for data collection in Hemorica are consistent with established datasets. An analysis of hemorrhage subtype distribution reveals that certain types—such as EPH, SAH, and SDH—occur less frequently in clinical settings, making them more challenging to diagnose. This phenomenon has also been observed in prior studies [60, 9]. The voxel-level distribution of hemorrhage shows that many lesions are relatively small, and hemorrhagic regions typically constitute only a minor portion of each CT volume. Heatmaps generated from the segmentation masks improve spatial understanding by highlighting the most common anatomical locations of hemorrhagic lesions. A comparison

between Hemorica and PhysioNet CT-ICH reveals notable differences in these heatmaps. These differences can largely be attributed to the underlying causes of hemorrhage, which vary between the patient populations in the two datasets. This conclusion is further supported by the differences in hemorrhage subtype distributions across the datasets. Moreover, the distribution of voxel intensities, as indicated by the Hounsfield Unit (HU) histogram, shows that hemorrhagic lesions in Hemorica generally appear brighter—or slightly brighter—than non-hemorrhagic regions. A similar pattern is observed in PhysioNet CT-ICH; however, in that dataset, a small number of lesions appear darker than the surrounding non-hemorrhagic tissue. Since the HU value of hemorrhagic regions is influenced by the age of the bleed, these variations may reflect differences in the timing of image acquisition relative to hemorrhage onset. Finally, the conditional probability matrix of hemorrhage subtypes reveals clinically meaningful co-occurrence patterns. Certain subtypes are more likely to appear together (e.g., ICH hemorrhage in conjunction with IVH hemorrhage), while other combinations are rarely observed. These relationships further support the diagnostic consistency and clinical relevance of the annotations provided in Hemorica.

While Hemorica provides a comprehensive and well-annotated resource for ICH research, several limitations should be acknowledged. First, the dataset is derived from a single institution—Rasoul Akram Hospital in Iran—which may limit the generalizability of models trained on it due to potential scanner-specific or population-specific biases. To enhance the diversity and robustness of the dataset, future versions could benefit from multi-center collaborations that include scans from different geographical regions and healthcare systems. Second, although the dataset includes 372 CT scans, the overall sample size remains relatively modest compared to large-scale datasets such as RSNA. Expansion of the dataset through the inclusion of additional cases and institutions would strengthen its utility for training deep learning models, particularly those with high capacity. Third, clinical metadata such as cause of accident, medical history, patient outcomes, time since symptom onset, and comorbidities are not included in the current version. The integration of such information in future releases would enable prognostic modeling and allow for more clinically meaningful applications.

Hemorica has been designed to support a wide range of research applications, and several use-cases are recommended to maximize its impact in the research community. Given its complete annotation structure—including classification, detection, and segmentation labels—it serves as an ideal benchmark for multi-task learning and hierarchical modeling. Researchers are encouraged to explore unified frameworks that can simultaneously or sequentially perform multiple tasks, reflecting the multi-dimensional nature of real-world clinical workflows. The dataset is also well-tailored for transfer learning and pre-training. Models trained on Hemorica can be fine-tuned on larger but weakly labeled datasets such as RSNA, improving sample efficiency and generalization. In addition, the segmentation masks offer opportunities for self-supervised or semi-supervised learning using unlabeled or partially labeled data.

Finally, two benchmark evaluations were conducted to assess the quality of the Hemorica, with a focus on general reproducible experiments aimed at gaining deeper insights into the characteristics of the dataset. The notable performance observed across both tasks confirms Hemorica’s reliability as a resource for ICH CT scan studies.

## 7 Conclusion

We present Hemorica, a novel, publicly accessible CT dataset for acute intracranial hemorrhage that overcomes key limitations of existing collections by providing slice- and patient-level subtype labels, bounding boxes, 2D masks, and 3D voxel annotations alongside hemorrhage volume estimates. Through detailed statistical comparisons and baseline benchmarks in classification, detection, and segmentation, we demonstrate that Hemorica not only matches real-world clinical distributions but also supports robust, interpretable AI model development with minimal architectural tuning. Our evaluation approved by medical experts confirms the dataset’s clinical validity, while its comprehensive annotation hierarchy enables transfer, self-supervised, and curriculum-learning strategies on larger, weakly labeled cohorts. Future work will focus on expanding Hemorica via multi-center collaborations and enriching it with patient metadata to further enhance its utility for prognostic modeling and broader neurological research.

### **Declaration of using Generative AI technologies in the writing process.**

During manuscript preparation, the authors used Grammarly to refine the paper’s clarity and language. They then reviewed and edited all material themselves and accept full responsibility for the content of this paper.

### **Acknowledgments**

The authors gratefully acknowledge the APAC Research Group for providing the computational infrastructure and hardware that made this work possible.

## References

- [1] Libo Xu, Zhenhao Wang, Wenchao Wu, Mao Li, and Qingsong Li. Global, regional, and national burden of intracerebral hemorrhage and its attributable risk factors from 1990 to 2021: results from the 2021 global burden of disease study. *BMC public health*, 24(1):2426, 2024.
- [2] Sang Joon An, Tae Jung Kim, and Byung-Woo Yoon. Epidemiology, risk factors, and clinical features of intracerebral hemorrhage: an update. *Journal of stroke*, 19(1):3, 2017.
- [3] Steven Tenny and William Thorell. Intracranial hemorrhage. In *StatPearls [Internet]*. StatPearls Publishing, 2024.
- [4] Aswin Pai, Ajay Hegde, Rajesh Nair, and Girish Menon. Adult primary intraventricular hemorrhage: clinical characteristics and outcomes. *Journal of neurosciences in rural practice*, 11(4):623, 2020.
- [5] Monika Grewal, Muktabh Mayank Srivastava, Pulkit Kumar, and Srikrishna Varadarajan. Radnet: Radiologist level accuracy using deep learning for hemorrhage detection in ct scans. In *2018 IEEE 15th International Symposium on Biomedical Imaging (ISBI 2018)*, pages 281–284. IEEE, 2018.
- [6] Balraj M Monica Jenefer, K Senathipathi, Aarthi, and Annapandi. Detection and categorization of acute intracranial hemorrhage subtypes using a multilayer densenet-resnet architecture with improved random forest classifier. *Concurrency and Computation: Practice and Experience*, 34(22):e7167, 2022.
- [7] Sasank Chilamkurthy, Rohit Ghosh, Swetha Tanamala, Mustafa Biviji, Norbert G Campeau, Vasantha Kumar Venugopal, Vidur Mahajan, Pooja Rao, and Prashant Warier. Deep learning algorithms for detection of critical findings in head ct scans: a retrospective study. *The Lancet*, 392(10162):2388–2396, 2018.
- [8] Mohammad R Arbabshirani, Brandon K Fornwalt, Gino J Mongelluzzo, Jonathan D Suever, Brandon D Geise, Aalpen A Patel, and Gregory J Moore. Advanced machine learning in action: identification of intracranial hemorrhage on computed tomography scans of the head with clinical workflow integration. *NPJ digital medicine*, 1(1):9, 2018.
- [9] Peter D Chang, Edward Kuoy, Jack Grinband, Brent D Weinberg, Matthew Thompson, Richelle Homo, Jefferson Chen, Hermelinda Abcede, Mohammad Shafie, Leo Sugrue, et al. Hybrid 3d/2d convolutional neural network for hemorrhage evaluation on head ct. *American Journal of Neuroradiology*, 39(9):1609–1616, 2018.
- [10] Weicheng Kuo, Christian Hane, Pratik Mukherjee, Jitendra Malik, and Esther L Yuh. Expert-level detection of acute intracranial hemorrhage on head computed tomography using deep learning. *Proceedings of the National Academy of Sciences*, 116(45):22737–22745, 2019.
- [11] Murtadha D Hssayeni, Muayad S Croock, Aymen D Salman, Hassan Falah Al-Khafaji, Zakaria A Yahya, and Behnaz Ghoraani. Intracranial hemorrhage segmentation using a deep convolutional model. *Data*, 5(1):14, 2020.
- [12] Andrew F Voter, Ece Meram, John W Garrett, and John-Paul J Yu. Diagnostic accuracy and failure mode analysis of a deep learning algorithm for the detection of intracranial hemorrhage. *Journal of the American College of Radiology*, 18(8):1143–1152, 2021.
- [13] Nannan Yu, He Yu, Haonan Li, Nannan Ma, Chunai Hu, and Jia Wang. A robust deep learning segmentation method for hematoma volumetric detection in intracerebral hemorrhage. *Stroke*, 53(1):167–176, 2022.
- [14] Ping Hu, Haizhu Zhou, Tengfeng Yan, Hongping Miu, Feng Xiao, Xinyi Zhu, Lei Shu, Shuang Yang, Ruiyun Jin, Wenlei Dou, et al. Deep learning-assisted identification and quantification of aneurysmal subarachnoid hemorrhage in non-contrast ct scans: development and external validation of hybrid 2d/3d unet. *Neuroimage*, 279:120321, 2023.
- [15] MD Anouk Stein, Carol Wu, Chris Carr, George Shih, Jayashree Kalpathy-Cramer, Julia Elliott, kalpathy, Luciano Prevedello, MD Marc Kohli, Matt Lungren, Phil Culliton, Robyn Ball, and Safwan Halabi MD. Rsna intracranial hemorrhage detection. <https://kaggle.com/competitions/rsna-intracranial-hemorrhage-detection>, 2019. Kaggle.
- [16] Adam E Flanders, Luciano M Prevedello, George Shih, Safwan S Halabi, Jayashree Kalpathy-Cramer, Robyn Ball, John T Mongan, Anouk Stein, Felipe C Kitamura, Matthew P Lungren, et al. Construction of a machine learning dataset through collaboration: the rsna 2019 brain ct hemorrhage challenge. *Radiology: Artificial Intelligence*, 2(3):e190211, 2020.
- [17] Deguo Ma, Chen Li, Tianming Du, Lin Qiao, Dechao Tang, Zhiyu Ma, Liyu Shi, Guotao Lu, Qingtao Meng, Zhihao Chen, et al. Phe-sich-ct-ids: A benchmark ct image dataset for evaluation semantic segmentation, object detection and radiomic feature extraction of perihematomal edema in spontaneous intracerebral hemorrhage. *Computers in Biology and Medicine*, 173:108342, 2024.

[18] Murtadha Hssayeni, M Croock, A Salman, H Al-khafaji, Z Yahya, and B Ghoraani. Computed tomography images for intracranial hemorrhage detection and segmentation. *Intracranial hemorrhage segmentation using a deep convolutional model*. *Data*, 5(1):14, 2020.

[19] Lu Li, Meng Wei, Bo Liu, Kunakorn Atchaneyasakul, Fugen Zhou, Zehao Pan, Shimran A. Kumar, Jason Y. Zhang, Yuehua Pu, David S. Liebeskind, and Fabien Scalzo. Deep learning for hemorrhagic lesion detection and segmentation on brain ct images. *IEEE Journal of Biomedical and Health Informatics*, 25(5):1646–1659, 2021.

[20] Anna N Khoruzhaya, Tatiana M Bobrovskaya, Dmitriy V Kozlov, Dmitriy Kuligovskiy, Vladimir P Novik, Kirill M Arzamasov, and Elena I Kremneva. Expanded brain ct dataset for the development of ai systems for intracranial hemorrhage detection and classification. *Data*, 9(2):30, 2024.

[21] Eduardo Pontes Reis, Felipe Nascimento, Mateus Aranha, Fernando Mainetti Secol, Birajara Machado, Marcelo Felix, Anouk Stein, and Edson Amaro. Brain hemorrhage extended (bhx): Bounding box extrapolation from thick to thin slice ct images. *PhysioNet*, 101(23):e215–20, 2020.

[22] Antoine Spahr, Jennifer Stähle, Chunliang Wang, and Magnus Kajser. Label-efficient deep semantic segmentation of intracranial hemorrhages in ct-scans. *Frontiers in Neuroimaging*, 2:1157565, 2023.

[23] Biao Wu, Yutong Xie, Zeyu Zhang, Jinchao Ge, Kaspar Yaxley, Suzan Bahadir, Qi Wu, Yifan Liu, and Minh-Son To. Bhsd: A 3d multi-class brain hemorrhage segmentation dataset. In *International Workshop on Machine Learning in Medical Imaging*, pages 147–156. Springer, 2023.

[24] Yuchen Guo, Yuwei He, Jinhao Lyu, Zhanping Zhou, Dong Yang, Liangdi Ma, Hao-Tian Tan, Changjian Chen, Wei Zhang, Jianxing Hu, Dongshan Han, Guiguang Ding, Shixia Liu, Hui Qiao, Feng Xu, Xin Lou, and Qionghai Dai. Deep learning with weak annotation from diagnosis reports for detection of multiple head disorders: a prospective, multicentre study. *The Lancet Digital Health*, 4(8):e584–e593, Aug 2022.

[25] Antonios Thanellas, Hannes Peura, Mikko Lavinto, Jussi P. Posti, Antti J. Katila, Tommi Luostarinen, Markus T. Nieminen, Olivier Sebastien, Juhana Frantzén, Zoltán Zador, Peka J. Lindsberg, Turgut Tatlisumak, Daniel Strbian, and Tiina Sairanen. Development and external validation of a deep learning algorithm to identify and localize subarachnoid hemorrhage on ct scans. *Neurology*, 100(13):e1257–e1266, Mar 2023.

[26] Marco Colasurdo, Nir Leibushor, Ariadna Robledo, Viren Vasandani, Zean Aaron Luna, Abhijit S. Rao, Roberto Garcia, Visish M. Srinivasan, Sunil A. Sheth, Naama Avni, Moleen Madziva, Mor Berejick, Goni Sirota, Aielet Efrati, Avraham Meisel, Hashem Shaltoni, and Peter Kan. Automated detection and analysis of subdural hematomas using a machine learning algorithm. *Journal of Neurosurgery*, 138(4):1077–1084, Apr 2023.

[27] Ajay Patel, F.H.B.M. Schreuder, C.J.M. Klijn, Robert Gooijer, Kathleen M. van Nieuwenhuizen, Jeroen de Borst, Erwin J. van Dijk, Frank-Erik de Leeuw, Anil M. Tuladhar, Caroline Siegel, Nynke A. Maaijwee, Pieter C. Vos, Mischa Aalders, Marianne A.A. van Walderveen, W.P.Th.M. Mali, and Birgitta K. Velthuis. Intracerebral haemorrhage segmentation in non-contrast ct. *Scientific Reports*, 9(1):17858, Nov 2019.

[28] Rajat Dhar, Guido J. Falcone, Yukun Chen, Ali Hamzehloo, Charles J. Moomaw, Stephan A. Mayer, David M. Schnyer, Chelsea S. Kidwell, Angela C. Leisure, Dinesh Chaudhary, M. Affan, Kellie Schwarz, Fernando D. Testai, John Muschelli, Joseph P. Broderick, M. James, Marsha Navratil, Marco Pasi, Anand Viswanathan, Christopher D. Anderson, and Kevin N. Sheth. Deep learning for automated measurement of hemorrhage and perihematomal edema in supratentorial intracerebral hemorrhage. *Stroke*, 51(2):648–651, Feb 2020.

[29] Nicholas Ironside, Ching J. Chen, Simukayi Mutasa, Nabil Simaan, Stephan A. Mayer, Lowell H. Sansing, E. Sander Connolly, Philip M. Meyers, Sean D. Lavine, Michael C. Barbour, Kevin N. Sheth, and Jun Huang. Fully automated segmentation algorithm for hematoma volumetric analysis in spontaneous intracerebral hemorrhage. *Stroke*, 50(12):3416–3423, Dec 2019.

[30] Valentina Abramova, Anna Clèrigues, Ana Quiles, Arnau Oliver, Xavier Lladó, Arzu Cöltekin, Dmitriy Lachinov, Miguel Castellanos, Michael Iv, Max Wintermark, and Miguel A. Pérez. Hemorrhagic stroke lesion segmentation using a 3d u-net with squeeze-and-excitation blocks. *Computerized Medical Imaging and Graphics*, 90:101908, Oct 2021.

[31] Yong En Kok, Stefan Pszczolkowski, Zhe Kang Law, Azlinawati Ali, Kannikanthan Krishnan, Philip M. Bath, Nikola Sprigg, Geoffrey C. Cloud, Neshika Samarasekera, Hester F. Lingsma, Stijn Fonville, Yvo B. Roos, Michel de Jong, Michel Muller, Hester F. Lingsma, Aad van der Lugt, Robert Allison, Eric Zeestraten, Lejla Alice, Rajiv Gupta, and Hester F. Lingsma. Semantic segmentation of spontaneous intracerebral hemorrhage, intraventricular hemorrhage, and associated edema on ct images using deep learning. *Radiology: Artificial Intelligence*, 4(6):e220096, Nov 2022.

[32] Xianjing Zhao, Kaixing Chen, Ge Wu, Guyue Zhang, Xin Zhou, Chuanfeng Lv, Shiman Wu, Yun Chen, Guotong Xie, and Zhenwei Yao. Deep learning shows good reliability for automatic segmentation and volume measurement

of brain hemorrhage, intraventricular extension, and peripheral edema. *European Radiology*, 31(7):5012–5020, Jul 2021.

[33] Nadine A. Coorens, Kevin G. Lipman, Sanjith P. Krishnam, Can Ozan Tan, Lejla Alic, and Rajiv Gupta. Intracerebral hemorrhage segmentation on noncontrast computed tomography using a masked loss function u-net approach. *Journal of Computer Assisted Tomography*, 47(1):93–101, Feb 2023.

[34] Maimaitijiang Nijiati, Alim Tuersun, Yimin Zhang, Memetjan Abliz, Kaibin Ding, and Aynur Seyiti. A symmetric prior knowledge based deep learning model for intracerebral hemorrhage lesion segmentation. *Frontiers in Physiology*, 13, Oct 2022.

[35] Aniwat Phaphuangwittayakul, Yi Guo, Fangli Ying, Ahmad Yahya Dawod, Salita Angkurawaranon, and Chaisiri Angkurawaranon. An optimal deep learning framework for multi-type hemorrhagic lesions detection and quantification in head ct images for traumatic brain injury. *Applied Intelligence*, 52(7):7320–7338, Jul 2022.

[36] Nikolai Schmitt, Yasin Mokli, Cornelia S. Weyland, Christian Zimmer, Julian Bösel, Jonathan Alexander Pfaff, Daniel Behme, Wenlu Zi, Simon Nagel, Karl Georg Haeusler, Franziska Dorn, Thomas Gerhard Liman, Stefan Schönenberger, Peter A. Ringleb, Martin Bendszus, and Markus A. Möhlenbruch. Automated detection and segmentation of intracranial hemorrhage suspect hyperdensities in non-contrast-enhanced ct scans of acute stroke patients. *European Radiology*, 32(4):2246–2254, Apr 2022.

[37] R. Austin Rava, Stanley E. Seymour, Mary Elizabeth LaQue, James J. Cook, Kyle M. Fargen, Adam S. Arthur, Sameer Ansari, Alejandro M. Spiotta, and Maxim Mokin. Assessment of an artificial intelligence algorithm for detection of intracranial hemorrhage. *World Neurosurgery*, 150(Jun):e209–e217, Jun 2021.

[38] JJ Heit, H Coelho, FO Lima, MF Granja, A Aghaebrahim, RA Hanel, E Sauvageau, AR Al-Bayati, RT Kellogg, JT Fifi, KS Handlogten, BM Howard, SA Ansari, W Qiu, and M Wintermark. Automated cerebral hemorrhage detection using rapid. *American Journal of Neuroradiology*, 42(2):273–278, Feb 2021.

[39] P. D. Chang, E. Kuoy, J. Grinband, B. D. Weinberg, M. Thompson, R. Homo, J. Chen, H. Abcede, M. Shafie, L. Sugrue, C. G. Filippi, M.-Y. Su, W. Yu, C. Hess, and D. Chow. Hybrid 3d/2d convolutional neural network for hemorrhage evaluation on head ct. *American Journal of Neuroradiology*, 39(9):1609–1616, Jul 2018.

[40] Hyunkwang Lee, Sehyo Yune, Mojdeh Mansouri, Misung Kim, Selar Tajmir, Claude Guerrier, Samuel Ebert, Shaun R. Pomerantz, Jose M. Romero, Sharmila Kamalian, Jay Patel, Robert W. Viggiano, Katherine P. Andriole, Adam G. Park, Sungmin Do, Jayashree Kalpathy-Cramer, Dong Bang, Yoonjung Yoo, B. J. Choi, and Ernest Lo. An explainable deep-learning algorithm for the detection of acute intracranial haemorrhage from small datasets. *Nature Biomedical Engineering*, 3(3):173–182, Mar 2019.

[41] Deniz Alis, Ceren Alis, Murat Yergin, Burcu Samanci, Ahmet Selim Kocaman, Burak Kilinc, Mehmet Ali Astarciooglu, Orhun Menekse, Tamer Ones, Salim Kara, Ozlem Goruroglu Ozturk, Neslihan Marashli, Efe Efendioglu, Filiz Turk, Mustafa Coskun, and Oya Onbas. A joint convolutional-recurrent neural network with an attention mechanism for detecting intracranial hemorrhage on noncontrast head ct. *Scientific Reports*, 12(1):2084, Feb 2022.

[42] James McLouth, Skyler Elstrott, Yassin Chaibi, Prabesh Sitoula, Ruben F. Barajas, J. Ramon Boto, Douglass Maye, and Christian G. Filippi. Validation of a deep learning tool in the detection of intracranial hemorrhage and large vessel occlusion. *Frontiers in Neurology*, 12, Jun 2021.

[43] Ali Arab, Betty Chinda, George Medvedev, William Siu, Hui Guo, Tao Gu, Sylvain Moreno, Ghassan Hamarneh, Martin Ester, and Xiaowei Song. A fast and fully-automated deep-learning approach for accurate hemorrhage segmentation and volume quantification in non-contrast whole-head ct. *Scientific Reports*, 10(1):19389, Nov 2020.

[44] Ning Yu, Hang Yu, Huijun Li, Lijun Ma, Mingfeng Zhang, Shaofa Xu, Weijing Liao, Kai Huang, Sanglin Ju, Hanbo Ren, and Jianming Liu. A robust deep learning segmentation method for hematoma volumetric detection in intracerebral hemorrhage. *Stroke*, 53(1):167–176, Jan 2022.

[45] Andriy Fedorov, Reinhard Beichel, Jayashree Kalpathy-Cramer, Julien Finet, Jean-Christophe Fillion-Robin, Sonia Pujol, Christian Bauer, Dominique Jennings, Fiona Fennelly, Milan Sonka, John Buatti, Stephen Aylward, James Miller, Steve Pieper, and Ron Kikinis. 3d slicer as an image computing platform for the quantitative imaging network. *Magnetic Resonance Imaging*, 30(9):1323–1341, November 2012.

[46] Ron Kikinis, Steve D Pieper, and Kirby G Vosburgh. 3d slicer: a platform for subject-specific image analysis, visualization, and clinical support. In *Intraoperative imaging and image-guided therapy*, pages 277–289. Springer, 2013.

[47] Olga Russakovsky, Jia Deng, Hao Su, Jonathan Krause, Sanjeev Satheesh, Sean Ma, Zhiheng Huang, Andrej Karpathy, Aditya Khosla, Michael Bernstein, Alexander C. Berg, and Li Fei-Fei. ImageNet Large Scale Visual Recognition Challenge. *International Journal of Computer Vision (IJCV)*, 115(3):211–252, 2015.

- [48] Kaiming He, Xiangyu Zhang, Shaoqing Ren, and Jian Sun. Deep residual learning for image recognition, 2015.
- [49] Gao Huang, Zhuang Liu, Laurens Van Der Maaten, and Kilian Q Weinberger. Densely connected convolutional networks. In *Proceedings of the IEEE conference on computer vision and pattern recognition*, pages 4700–4708, 2017.
- [50] Mingxing Tan and Quoc V. Le. Efficientnet: Rethinking model scaling for convolutional neural networks, 2020.
- [51] Ze Liu, Han Hu, Yutong Lin, Zhuliang Yao, Zhenda Xie, Yixuan Wei, Jia Ning, Yue Cao, Zheng Zhang, Li Dong, Furu Wei, and Baining Guo. Swin transformer v2: Scaling up capacity and resolution, 2022.
- [52] Sachin Mehta and Mohammad Rastegari. Mobilevit: Light-weight, general-purpose, and mobile-friendly vision transformer. In *Proc. of the International Conference on Learning Representations (ICLR)*, 2022. arXiv preprint arXiv:2110.02178.
- [53] Saining Xie, Ross Girshick, Piotr Dollár, Zhuowen Tu, and Kaiming He. Aggregated residual transformations for deep neural networks, 2017.
- [54] Jie Hu, Li Shen, Samuel Albanie, Gang Sun, and Enhua Wu. Squeeze-and-excitation networks, 2019.
- [55] Christopher M. Bishop. *Pattern Recognition and Machine Learning*, volume 4. Springer, 2006.
- [56] Diederik P. Kingma and Jimmy Ba. Adam: A method for stochastic optimization. *arXiv preprint arXiv:1412.6980*, 2014.
- [57] Olaf Ronneberger, Philipp Fischer, and Thomas Brox. U-net: Convolutional networks for biomedical image segmentation, 2015.
- [58] Hengshuang Zhao, Jianping Shi, Xiaojuan Qi, Xiaogang Wang, and Jiaya Jia. Pyramid scene parsing network, 2017.
- [59] Amir Hillal, Teresa Ullberg, Birgitta Ramgren, and Johan Wassélius. Computed tomography in acute intracerebral hemorrhage: neuroimaging predictors of hematoma expansion and outcome. *Insights into imaging*, 13(1):180, 2022.
- [60] Hai Ye, Feng Gao, Youbing Yin, Danfeng Guo, Pengfei Zhao, Yi Lu, Xin Wang, Junjie Bai, Kunlin Cao, Qi Song, et al. Precise diagnosis of intracranial hemorrhage and subtypes using a three-dimensional joint convolutional and recurrent neural network. *European radiology*, 29:6191–6201, 2019.